



HAL
open science

Topology optimization of the electrodes in dielectrophoresis-based devices

Abbas Homyouni Amlashi, Laure Koebel, Alexis Lefevre, Abdenbi Mohand Ousaid, Aude Bolopion

► **To cite this version:**

Abbas Homyouni Amlashi, Laure Koebel, Alexis Lefevre, Abdenbi Mohand Ousaid, Aude Bolopion. Topology optimization of the electrodes in dielectrophoresis-based devices. *Computers & Structures*, 2024, 301, pp.107444. 10.1016/j.compstruc.2024.107444 . hal-04693050

HAL Id: hal-04693050

<https://hal.science/hal-04693050>

Submitted on 10 Sep 2024

HAL is a multi-disciplinary open access archive for the deposit and dissemination of scientific research documents, whether they are published or not. The documents may come from teaching and research institutions in France or abroad, or from public or private research centers.

L'archive ouverte pluridisciplinaire **HAL**, est destinée au dépôt et à la diffusion de documents scientifiques de niveau recherche, publiés ou non, émanant des établissements d'enseignement et de recherche français ou étrangers, des laboratoires publics ou privés.

Topology Optimization of the Electrodes in Dielectrophoresis-Based Devices

Abbas Homayouni-Amlashi*, Laure Koebel, Alexis Lefevre, Abdenbi Mohand-Ousaid, and Aude Bolopion

^aFEMTO-ST Institute, CNRS, Univ. Bourgogne Franche-Comté, AS2M department, 24 rue Alain Savary, Besançon, 25000, Bourgogne Franche-Comté, France

Abstract

1 This paper aims for developing topology optimization methodology to design the shape of electrodes in Di-
2 electrophoresis (DEP)-based devices. The DEP force is due to a non-uniform electric field induced by applied
3 voltages to the electrodes. Shape of the electrodes has the principal effect on the direction and magnitude of
4 the DEP force. In medical therapy microfluidic devices, DEP force is used for cell sorting and cell separation.
5 While the direction and magnitude of the DEP force are desired to be determined and maximized respec-
6 tively, the magnitude of the electric field should be minimized to avoid damaging cells. Approaching these
7 goals is counter intuitive where the existing electrode designs are basic. Therefore, a detailed finite element
8 model (FEM) is developed for DEP force and electric field to formulate an optimization problem to maxi-
9 mize the DEP force in a particular direction while there is a constraint on electric field's magnitude. Using
10 the developed FEM, explicit formulations for sensitivity analysis are derived to implement a gradient-based
11 topology optimization. The performance of developed methodology is assessed numerically to determine
12 the direction of the DEP force and constraining the electric field and experimentally in a practical case study
13 of particle trapping in a microfluidic channel.

Keywords: Dielectrophoresis, Topology optimization, Sensitivity analysis, Electrode design, Microfluidic Devices

1. Introduction

14 DEP is a phenomenon that is primarily found by Pohl. et al [1] in which a force is applied on a polar-
15 izable particle inside a non-uniform electric field. This force is used to manipulate, control [2, 3] and sort
16 the particles flowing inside a fluid. DEP has application interests in micro-manipulation [4] cell sorting and
17 medical therapy devices and is crucial in drug efficacy evaluation, cancer diagnostics [5] and cell replace-
18 ment therapy [6]. The magnitude of DEP force depends on the gradient of the electric field which can be
19 produced by the application of AC or DC voltage on a designed electrode. In this case, the magnitude and
20 direction of the DEP force rely on the shape and geometry of the electrode. Therefore, various shapes for the
21 electrodes are proposed including parallel [7], interdigitated [8], castellated [9], quadrupole [10], annular
22 [11], oblique [12], curved [13], etc. A brief review of each of these designs is reported in [14].

23 Recently, optimization approaches have been used to design more efficient electrodes. The optimization
24 methods include investigative approach on the basic shapes of the electrodes like rectangular, trapezoidal,
25 etc. [15], different placement of rectangular electrodes [16], shape optimization using genetic algorithm
26 [17, 18] and microelectrode discretization [19]. In these optimization approaches, the main drawback is
27 that due to the heavy computational time, large rectangular blocks are employed to discretize the design
28 domain for the electrodes. This will restrict the complexity and diversity of the obtained geometry of the
29 electrodes. Indeed, the discretization of the design domain for the electrodes in these researches is more
30 coarse than the regular discretization in the finite element approach. The study which optimizes the shape
31 of the electrodes based on the finite element discretization is the work done by Yoon et al. [20] in which

Email address: abbas.homayouni@femto-st.fr (Abbas Homayouni-Amlashi*)

32 the topology optimization methodology is introduced as a potential methodology to optimize the shape
33 of the electrodes. However, in this study, the sensitivity analysis which is a crucial part of the gradient-
34 based topology optimization methodology is not formulated. The lack of sensitivity analysis makes the
35 computation time extremely high for gradient based solvers. In addition, the efficiency of the obtained
36 optimized shape of the electrodes is not investigated experimentally. More importantly, constraining the
37 magnitude of the electric field is not addressed in the optimization formulation of the aforementioned
38 optimization approaches in the literature. Limiting the magnitude of the electric field is hugely important in
39 medical therapy microfluidic devices since a high electric field can kill living cells [21]. To limit the electric
40 field, reduction of input voltage is not an efficient solution since there is a nonlinear relationship between the
41 DEP force and electric field. Producing novel shapes of the electrodes for accurate control of the direction of
42 the DEP force and controlling the magnitude of the electric field can be achieved by topology optimization
43 methodology.

44 Topology optimization is a form of structural optimization based on finite element discretization which
45 distributes the material inside a design domain in an optimal way while there is no prior knowledge of the
46 final optimal layout. This methodology is an algorithmic approach in which the design domain will evolve
47 to the final optimal layout in a sequence of iterations. Topology optimization methodology is primarily
48 proposed for mechanical compliance problems in which the idea was to minimize the deformation of a me-
49 chanical structure [22, 23]. When the methodology is well established in the literature [24], it has been
50 applied to various physics including the thermal and heat transfer [25, 26], fluid dynamics [27], aerodynam-
51 ics [28], optics [29], piezoelectricity [30, 31, 32], electromagnetic [33], etc. Indeed, the interest in using
52 topology optimization is its ability to produce complex designs where intuitive or trial-error approaches are
53 either impossible or inefficient.

54 In this paper, the topology optimization methodology in particular the SIMP (Solid Isotropic Material
55 with Penalization) approach has been used to optimize the shape of the electrodes in DEP-based devices.
56 First, a detailed FEM is established to model the electric field and DEP force. The optimization problem is
57 formulated to precisely determine the direction of the DEP force and to put a constraint on the magnitude of
58 the electric field. Due to high resolution of the FEM discretization, the number of optimization variables is
59 very high in topology optimization and hence the gradient-based solvers like Method of Moving Asymptotes
60 (MMA) [34, 35] are generally used to solve the optimization problem. In this case, we need to provide the
61 sensitivity analysis in which the gradient of the objective function with respect to the optimization variables
62 is calculated. Thanks to the developed FEM, explicit formulations for sensitivity analysis are derived for DEP
63 force and electric field using the adjoint method. The sensitivity analysis is performed in a general format
64 so the methodology can be used for different DEP-based applications with minor modifications. COMSOL
65 multiphysics is used to verify the developed FEM and to verify the derived sensitivity analysis, the numerical
66 central difference method is used and the results of sensitivities from both methods are compared and
67 reported.

68 To investigate the performance of the developed methodology, a numerical investigation is performed
69 to study the efficiency of the methodology in terms of an accurate definition of the DEP force's direction
70 and to reduce the electric field in a desired zone. Moreover, a particular case study has been defined as
71 trapping the randomly distributed particles inside a desired convergence zone in a fluid flowing inside a
72 microdimensional channel. The optimization problem is defined to determine the direction of the DEP force
73 in the desired convergence zone. Two optimized electrodes with two different surface areas are obtained
74 from the developed topology optimization methodology. Then, these two optimized designs are transferred
75 to the COMSOL multiphysics platform for the simulation. The trapping efficiencies of the optimized designs
76 are compared with a U-shape design which has been designed for the same purpose [36] recently. Videos of
77 simulating the particle trapping performances of the designs are added as supplementary materials. In the
78 final step of the research, the optimized designs are fabricated on a fluidic chip and their performance in
79 trapping the beads inside the desired convergence zone is investigated experimentally. The video recordings
80 of experimentation which demonstrate the performance of different designs in terms of particle trapping are
81 provided as supplementary materials.

82 The paper is organized as follows: Section 2 is devoted to the modeling of the system which starts with
83 the definition of the DEP force and is followed by a detailed FEM which will be used in section 3 for the

84 implementation of topology optimization. In section 3, the SIMP approach is implemented, the optimization
 85 problem is formulated and sensitivity analysis is performed. In section 4, the performance of the developed
 86 methodology is examined in several numerical case studies to determine the direction of the DEP force and
 87 constraining the electric field. In section 5, a case study is defined to assess the performance of the developed
 88 methodology for particle trapping inside a microfluidic chip. In section 6, the results of the optimization
 89 algorithm written in MATLAB are presented. In section 7, the obtained electrode designs are validated
 90 primarily by simulation in the COMSOL multiphysics platform and later by experimental investigation. There
 91 will be a discussion on the results and methodology in section 8, and finally, the conclusion of the work is
 92 presented. The fabrication process and description of the experimental setup are provided in the appendix.

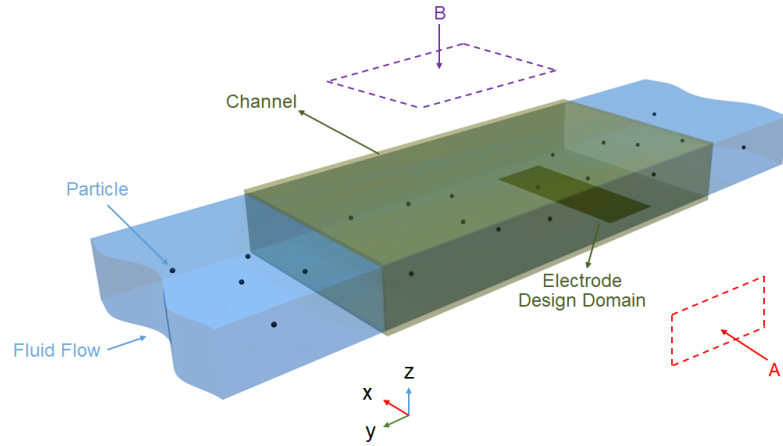


Figure 1: Overview of the fluid containing particles at random positions flowing inside a channel

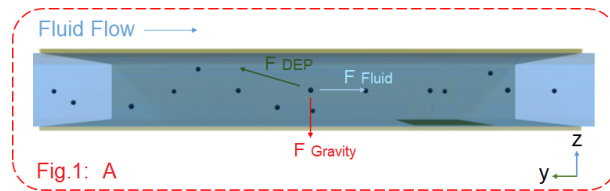


Figure 2: Forces on a particle inside a fluid with non-uniform electric field

93 2. Modeling

94 Consider a fluid containing randomly distributed particles flowing inside a channel as it is illustrated in
 95 Fig. 1. At the bottom of the channel, there are electrodes with unknown geometry. These electrodes apply
 96 DEP forces on the particles inside the fluid by producing a non-uniform electric field. Particles inside the fluid
 97 flow are under the application of various forces which are illustrated in Fig. 2. Regarding the introduced
 98 physic of interest, several assumptions are considered in modeling process without loss of generality:

- 99 • the gravity and fluidic forces are not considered in the physical modeling,
- 100 • particles are assumed to be spherical,
- 101 • mutual particle interactions are neglected,
- 102 • particle interactions with walls of the channel are neglected

103 First assumption is considered to focus on the DEP force. Second assumption simplifies modeling the
 104 DEP force. With third assumption, the study will be done on each particle solely without considering other
 105 particles' effects. With these assumptions, the general modeling of DEP force can be represented.

106 Any particle in a non-uniform electric field will experience an electrostatic force due to Maxwell's stress
 107 tensor. For a spherical particle, Maxwell's stress tensor generates a dielectrophoretic (DEP) force on the
 108 polarized particle that can be expressed as [37, 38]

$$F_{DEP} = 2\pi\epsilon_m r^3 \text{Re}(f_{CM}) \nabla |E|^2 \quad (1)$$

109 In which r is the radius of the particle, ϵ_m is the permittivity of the medium (fluid), ∇ is the vector
 110 differential operator and E is the electric field,

$$E = -\nabla\Phi \quad (2)$$

111 where Φ is the potential field. In addition, in equation (1), f_{CM} is the Clausius Mossotti factor that can be
 112 calculated as

$$f_{CM} = \frac{\epsilon_p^* - \epsilon_m^*}{\epsilon_p^* + 2\epsilon_m^*}$$

$$(\epsilon_p^* = \epsilon_p - j\frac{\sigma_p}{\omega}, \epsilon_m^* = \epsilon_m - j\frac{\sigma_m}{\omega}) \quad (3)$$

113 ϵ_p and σ_p are the permittivity and conductivity of the particle. σ_m is the conductivity of the fluid, ω is the
 114 frequency of the AC potential and $\{ * \}$ is the sign of a complex number. For the optimization target of this
 115 paper, just the real part of the ϵ is considered [20]. By inspecting the equation (1), it is obvious that the
 116 only term that affects the direction and magnitude of DEP force is the square of the electric field's gradient
 117 (i.e. $\nabla |E|^2$). This latter can be maximized or minimized by optimizing the shapes of the electrodes. To do
 118 so, an area of the channel will be considered as the design domain for the electrodes as it is illustrated in
 119 Fig. 3-(a). The modeling in this paper will be in 2D and the effects of the height of the channel are not
 120 considered which simplifies the computational burdensome. Although 2D modeling is an approximation
 121 considering the inherently three-dimensional nature of the problem, we will show in the simulation and
 122 experimental parts that when the height of the channel is sufficiently low the performance of the electrodes
 123 follows their 2D modeling. The 2D design domain is separated into two parts of fluid (white) and electrode
 124 (black). In addition, an area (Ω) is considered as target area in which the goal is to modify the magnitude
 125 and direction of the DEP force and electric field.

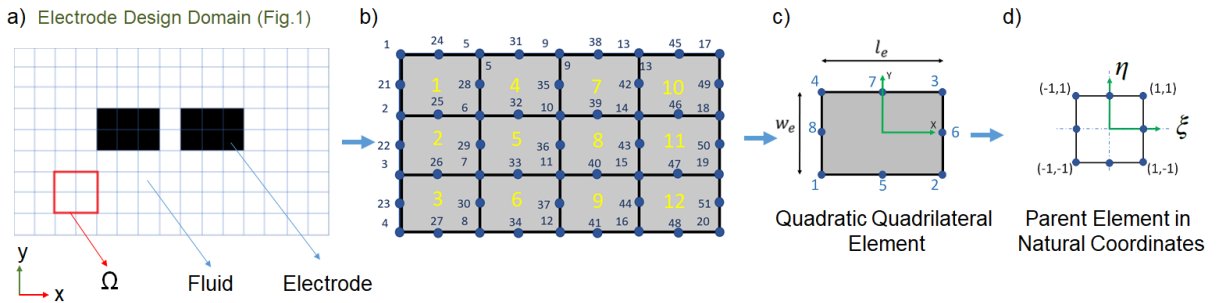


Figure 3: a) Finite element discretization of the design domain with quadratic quadrilateral elements (Ω : Target area) . b) Coarse discretization of design domain. c) Numbering format inside each element. d) Parent element in natural coordinates.

126 *2.1. Finite Element Model*

127 In Fig. 3, the design domain is discretized with finite number of elements. This is a coarse discretization
 128 of the design domain for illustrative purposes. From equations (1) and (2), it is obvious that for calculation
 129 of DEP force, two times derivative of the potential field is required. As such, the quadratic quadrilateral
 130 elements are used to discretize the design domain as it can be seen in Fig. 3-(b and c). These elements have
 131 8 nodes and each node holds a scalar value of potential as degree of freedom. Generally, these elements
 132 can have different length (l_e) and width (w_e) [39]. To facilitate the calculations, the parent element in the
 133 natural coordinates (ξ, η) is used as it is illustrated in Fig. 3-(d). The connectivity, assembly of elements and
 134 numbering format of the nodes and elements are illustrated in panel (b) of Fig. (3). This is helpful for the
 135 creation of the global dielectric matrix and final FEM of the system. To support the material presented in
 136 this section, more detailed finite element calculation is provided in the appendix. The provided concept will
 137 be later used in the modeling of the electric field, DEP force and sensitivity analysis of optimization section.

138 To build the finite element model, we start by expressing the Gauss law

$$\nabla \cdot (D) = Q \quad (4)$$

139 where D is the electric displacement vector, and Q is the electric charge. The boundary condition consists
 140 of Dirichlet ($\Phi = \Phi_c : \Phi_c = \text{constant potential}$) and Neumann conditions ($n \cdot \nabla \Phi = 0 : n = \text{normal vector of}$
 141 the border) [40] which will be explained here after discretizing the design domain. In addition we have the
 142 following relation between electric displacement vector (D) and electric field (E),

$$D = \varepsilon E \quad (5)$$

143 in which ε is the permittivity of the domain that in our paper can be electrode or fluid and it will be
 144 determined by the optimization algorithm. Now, by using equations (2, 4 and 5) and considering that the
 145 internal virtual work over one element is equal to the work done by the external electric charges over one
 146 element [41] the weak form of Gauss law can be written as,

$$\int_{\Omega^e} (\delta E^e)^T D^e d\Omega = -(\delta \phi^e)^T Q^e \quad (6)$$

147 in which, e is showing that the parameter belongs to the element, ϕ is the elemental potential vector, Q is
 148 the charge, δ is the variation sign and Ω^e is the area of one element. By having equation and from the basics
 149 of FEM, we can calculate the electric field over an element using the gradient interpolation matrix (B) as
 150 follows,

$$E = B\phi \quad (7)$$

151 Then the elemental dielectric matrix can be calculated as

$$k = \int_{\Omega^e} B^T \varepsilon B d\Omega \quad (8)$$

152 in which $|\bar{J}|$ is the determinant of the Jacobean matrix to map the coordinate system from global coordinate
 153 to the natural coordinate [42]. The integration over each element can be done using the numerical Gauss
 154 quadrature method [42]. Since the elements are quadratic, 3×3 Gauss points can be used to calculate the
 155 dielectric matrix with reasonable accuracy. The elemental equilibrium equation can be written as

$$k\phi = Q^e \quad (9)$$

156 The obtained elemental dielectric matrices for each element should be assembled to obtain the global
 157 dielectric matrix. By doing so, the global equilibrium equation in open circuit condition ($Q^e = 0$) can be
 158 written as

$$K\Phi = 0 \quad (10)$$

159 where K and Φ are the global dielectric matrix and vector of potentials respectively. To solve this equation,
 160 the potential values of some nodes should be known initially as Dirichlet boundary condition. Through these
 161 known values of potentials, the potential values of other nodes can be found with a procedure explained in
 162 [43, 44]. For the boundaries of the discretized domain, there is a Neumann boundary condition in which the
 163 gradient of potential is zero. The procedures of applying the Dirichlet and Neumann boundary conditions
 164 are also explained in [43, 44].

165 By applying the boundary conditions to the global equilibrium equation (10), the potential field will be
 166 obtained and the electric field can be evaluated by using equation (7),

$$\vec{E} = [B_x\phi] \vec{i} + [B_y\phi] \vec{j} \quad (11)$$

167 where \vec{i} and \vec{j} are the unit vectors in the direction of x and y coordinates system respectively.

168 For the calculation of DEP force based on equation (1), we need the gradient of the electric field which
 169 can be calculated as follows

$$\nabla|E|^2 = \frac{\partial}{\partial x}(E_x^2 + E_y^2)\vec{i} + \frac{\partial}{\partial y}(E_x^2 + E_y^2)\vec{j} \quad (12)$$

170 where in terms of finite element matrices, we have

$$\nabla|E|^2 = [2B_x\phi \cdot B_{xx}\phi + 2B_y\phi \cdot B_{yx}\phi] \vec{i} + [2B_x\phi \cdot B_{xy}\phi + 2B_y\phi \cdot B_{yy}\phi] \vec{j} \quad (13)$$

171 In which, the calculation of derivatives of gradient interpolation matrices (i.e. B_{xx} , B_{yy} and B_{xy}) is
 172 mentioned in appendix. By using equation (13), the DEP force in equation (1) can be calculated.

173 After developing the FEM for the electric field and the DEP force, it is possible to enter the optimization
 174 phase to design the shape of the electrodes.

175 3. Optimization

176 In this section, the goal is to optimize the shape of the electrode to maximize the DEP forces in a desired
 177 direction in the target area (Ω) to modify the particle's trajectory inside the fluidic channel. This desired
 178 direction can be in any direction based on the application. However, the procedure of deriving the sensitivity
 179 analysis remains the same for any other direction. In addition to direction, minimizing the magnitude of
 180 electric field is also important since it can damage the living cells. Therefore, the optimization problem
 181 should be formulated by definition of the objective function, constraints and optimization variables. These
 182 terms will be defined in the following sections.

183 3.1. Objective Definition

To define the optimization problem in a general format, we can consider a target area (Ω) in the design
 domain (Fig. (3)-(a)) in which the goal is to maximize or minimize the DEP force in a particular direction

and maximize or minimize the magnitude of electric field. Therefore, We have to define cost functions for DEP force and electric field. For DEP force, let's suppose that the goal is to maximize the DEP force in the x direction then the cost function can be defined as

$$\bar{G}_{x-\Omega} = - \int_{\Omega} \frac{\partial}{\partial x} (E_x^2 + E_y^2) d\Omega \quad (14)$$

184 The cost function in (14) is defined similar to the Ref. [20]. However, in this reference, the method for
 185 calculation of this integration which is essential for the sensitivity analysis has not been provided. Here, we
 186 use the natural coordinates and the Gauss points which are introduced in the previous sections to calculate
 187 the cost functions and to perform the sensitivity analysis in the next section. To calculate the integration
 188 (14) over the area of each element, the design domain is already discretized to a finite number of elements.
 189 Since the elements are quadratic, 3×3 Gauss points are used for accurate approximation of the integral
 190 values. As such, by using the equations (45-13), the integration in equation (14) can be calculated,

$$\bar{G}_{x-\Omega} = \sum_e \sum_{i=1}^3 \sum_{j=1}^3 W_i W_j \left[2B_x(\xi_i, \eta_j) \phi B_{x,x}(\xi_i, \eta_j) \phi + 2B_y(\xi_i, \eta_j) \phi B_{y,x}(\xi_i, \eta_j) \phi \right] |\bar{J}| \quad (15)$$

191 In equation (15), $\nabla|E|^2$ is calculated on each Gauss points (ξ_i and η_j) and the inner summations by Gauss
 192 weighting factors W_i and W_j [42, 45], give an scalar value for the integration of $\nabla|E|^2$ over one element (e).
 193 Then, the external summation calculates the sum of $\nabla|E|^2$ for all the elements inside the target area. Having
 194 a scalar value of $\nabla|E|^2$ for each element is necessary for performing the sensitivity analysis.

195 To modify the magnitude of the electric field over the target area (Ω), the following integration of the
 196 Euclidean norm is introduced here,

$$\bar{E}_{\Omega} = \int_{\Omega} (E_x^2 + E_y^2) d\Omega \quad (16)$$

197 where \bar{E}_{Ω} represents the sum of the square of electric field's magnitude over a target area (Ω). By using
 198 equation (11) and the numerical Gauss quadrature, we can rewrite the variable \bar{E}_{Ω} as

$$\bar{E}_{\Omega} = \sum_e \sum_{i=1}^3 \sum_{j=1}^3 W_i W_j \left[2\phi^T B_x^T(\xi_i, \eta_j) B_x(\xi_i, \eta_j) \phi + 2\phi^T B_y^T(\xi_i, \eta_j) B_y(\xi_i, \eta_j) \phi \right] |\bar{J}| \quad (17)$$

199 The objective function can be defined as the weighted sum of the $\bar{G}_{x-\Omega}$ and $\bar{G}_{y-\Omega}$ to determine the
 200 direction of the DEP force and we can consider \bar{E}_{Ω} as a constraint. This will be discussed in the formulation
 201 of optimization problem.

202 After establishing the finite element model and defining the objective function, the SIMP topology opti-
 203 mization approach can be developed for the physic of interest.

204 3.2. SIMP topology optimization

205 There are several approaches to apply the topology optimization methodology [46]. Among them, the
 206 SIMP approach which stands for Solid Isotropic Material with Penalization is more popular due to its effi-
 207 ciency and simplicity of implementation. The core concept of the SIMP topology optimization is the material
 208 interpolation function which attributes a continuous variable to each element in the design domain to relax
 209 a particular property of the material from a binary value to a continuous one [24]. To better understand the
 210 SIMP topology optimization algorithm, the implementation steps will be explained in the coming sections.

211 *3.2.1. Material interpolation scheme*

212 To apply the SIMP approach, a material interpolation function is used to attribute a permittivity to
 213 each element inside the design domain. The permittivities of elements are relaxed to variate between the
 214 permittivity of fluid (ε_{min}) and permittivity of conductive electrode (ε_0) in the sequence of optimization
 215 iterations. This steering will form the shape of the electrode after the optimization. The optimization
 216 variable is a continuous value between zero and one which will be multiplied to the permittivity of the
 217 material. This material interpolation scheme can be interpreted as follows [24, 20]

$$k(\gamma) = (\varepsilon_{min} + \gamma^p(\varepsilon_0 - \varepsilon_{min}))\bar{k}, \quad 0 < \gamma \leq 1 \quad (18)$$

218 In this equation, p is the penalization factor and variable γ is the optimization variable that varies
 219 between a very low value to the maximum value of one. The normalized elemental dielectric matrix \bar{k}
 220 is defined by factorization of the permittivity from equation (8)

$$\bar{k} = \int_{\Omega^e} B^T B d\Omega \quad (19)$$

221 The normalized dielectric matrix in equation (19) will be used in the material interpolation equation
 222 (18) to form a continuous dielectric matrix. The material interpolation function in equation (18) can also
 223 be interpreted by the color spectrum of the design domain where the black color shows the electrode which
 224 has the maximum permittivity while the white color shows the fluid with the lowest permittivity. In the iter-
 225 ative sequence of the SIMP optimization algorithm, the elements start from intermediate permittivity (gray
 226 elements) and will be steered to the electrode (black elements) or fluid (white elements) permittivities and
 227 finally form the shape of the electrode. In this paper, the permittivity of conductive electrode is considered
 228 to be 1000 times bigger than the permittivity of fluid.

229 To steer the optimization variables to zero or one in an optimal way, we need a solution method to
 230 update these variables through the iterations. Since we are dealing with a nonlinear optimization problem
 231 with high numbers of variables, gradient-based numerical methods will be used as updating algorithm. In
 232 this regard, the gradient of the objective function with respect to optimization variables which is known as
 233 sensitivity analysis is necessary and will be provided in the next section.

234 *3.2.2. Sensitivity analysis (DEP force)*

235 To perform a gradient-based optimization, the sensitivity of the objective function with respect to the
 236 permittivity should be calculated. The problem that emerges here is that the gradient of the potential vector
 237 with respect to the design variable is not available (i.e. $\frac{\partial \phi}{\partial \gamma}$). To remedy, the adjoint method can be used
 238 to avoid the derivation of the potential vector [24, 41]. By using the adjoint method, we augment the
 239 equilibrium equation (10) to the objective function (14) using the global adjoint vector Υ which will not
 240 change the value of the objective function. In this manner, the integration (15) can be reformulated as
 241 follows

$$\bar{G}_{x-\Omega} = \Upsilon^T K \Phi + \sum_e \sum_{i=1}^3 \sum_{j=1}^3 W_i W_j \left[2\phi^T B_x^T(\xi_i, \eta_j) B_{x,x}(\xi_i, \eta_j) \phi + 2\phi^T B_y^T(\xi_i, \eta_j) B_{y,x}(\xi_i, \eta_j) \phi \right] |\bar{J}| \quad (20)$$

242 Now, the sensitivity analysis can be formulated by derivation of the augmented objective function 20
 243 with respect to the optimization variable γ

$$\begin{aligned} \bar{G}'_{x-\Omega} = & \lambda^T k \phi' + \lambda^T k' \phi + \sum_e \sum_{i=1}^3 \sum_{j=1}^3 W_i W_j \left[2\phi^T (B_x^T(\xi_i, \eta_j) B_{x,x}(\xi_i, \eta_j) + \right. \\ & \left. B_{x,x}^T(\xi_i, \eta_j) B_x(\xi_i, \eta_j)) \phi' + 2\phi^T (B_y^T(\xi_i, \eta_j) B_{y,x}(\xi_i, \eta_j) + B_{y,x}^T(\xi_i, \eta_j) B_y(\xi_i, \eta_j)) \phi' \right] |\bar{J}| \end{aligned} \quad (21)$$

244 Here, ' is the derivation with respect to optimization variable (i.e. $\frac{\partial}{\partial y}$), λ is the adjoint vector in the
245 elemental level. Moreover, there is a remark about the matrix derivation that has been taken into account
246 for the derivation of sensitivity (21):

Remark: suppose that we have a scalar value M , which is defined as

$$M = X^T A X \quad (22)$$

When X is a vector and function of variable z and A is a nonsymmetric square matrix and it is not a function of variable z , then,

$$\frac{\delta M}{\delta z} = X^T (A + A^T) \frac{\delta X}{\delta z} \quad (23)$$

247 Now to avoid the calculation of ϕ' , we have to solve the following adjoint equation

$$\begin{aligned} \Upsilon^T K + \sum_e \sum_{i=1}^3 \sum_{j=1}^3 W_i W_j \left[2\phi^T (B_x^T(\xi_i, \eta_j) B_{x,x}(\xi_i, \eta_j) + \right. \\ \left. B_{x,x}^T(\xi_i, \eta_j) B_x(\xi_i, \eta_j)) + 2\phi^T (B_y^T(\xi_i, \eta_j) B_{y,x}(\xi_i, \eta_j) + B_{y,x}^T(\xi_i, \eta_j) B_y(\xi_i, \eta_j)) \right] |\bar{J}| = 0 \end{aligned} \quad (24)$$

248 The adjoint equation (24) should be solved at the global level. To do so, it can be rewritten in the
249 following format,

$$\begin{aligned} \Upsilon^T K + \sum_e \phi^T \left[\sum_{i=1}^3 \sum_{j=1}^3 W_i W_j \left[2(B_x^T(\xi_i, \eta_j) B_{x,x}(\xi_i, \eta_j) + \right. \right. \\ \left. \left. B_{x,x}^T(\xi_i, \eta_j) B_x(\xi_i, \eta_j)) + 2(B_y^T(\xi_i, \eta_j) B_{y,x}(\xi_i, \eta_j) + B_{y,x}^T(\xi_i, \eta_j) B_y(\xi_i, \eta_j)) \right] \right] |\bar{J}| = 0 \end{aligned} \quad (25)$$

250 Now we can define,

$$\left[\sum_{i=1}^3 \sum_{j=1}^3 W_i W_j \left[(B_x^T(\xi_i, \eta_j) B_{x,x}(\xi_i, \eta_j) + B_{x,x}^T(\xi_i, \eta_j) B_x(\xi_i, \eta_j) + B_y^T(\xi_i, \eta_j) B_{y,x}(\xi_i, \eta_j) + B_{y,x}^T(\xi_i, \eta_j) B_y(\xi_i, \eta_j)) \right] \right] = \mathbf{B}_{x,e} \quad (26)$$

251 The matrix $\mathbf{B}_{x,e}$ is a square and symmetric matrix at the elemental level with an equivalent size to the
252 elemental dielectric matrix (k). Therefore, with a similar method, it can be assembled to obtain a global
253 matrix as,

$$\sum_e \mathbf{B}_{x,e} = \mathbb{B}_x \quad (27)$$

254 The assembly procedure of the elemental matrix to obtain the global matrix is explained step by step in

255 the MATLAB codes published for topology optimization [47, 32]. Now by using the global matrix in equation
 256 (27), the global adjoint equation can be solved as follows,

$$\Upsilon^T K = \Phi^T \mathbb{B}_x \quad (28)$$

257 By calculation of the adjoint vector at the global level, it should be dissolved to the elemental level to
 258 be used in the sensitivity function. The conversion of the global adjoint vector to the elemental adjoint
 259 vector can be done with the help of the connectivity matrix [47] which is used in the assembly procedure of
 260 the elemental to global matrices. The detailed procedure can be found in the MATLAB codes published by
 261 authors [32]. Finally, the sensitivity equation can be derived as

$$\bar{G}'_{x-\Omega} = \lambda^T k' \phi \quad (29)$$

262 To obtain the sensitivity, the derivative of the dielectric matrix with respect to the design variable is
 263 required as well. By using the material interpolation scheme in equation (18), the derivative of the dielectric
 264 matrix can be calculated as

$$k' = p\gamma^{(p-1)}(\varepsilon_0 - \varepsilon_{min})\bar{k} \quad (30)$$

265 Equations (28 & 29 & 30) form the explicit formulation for the sensitivity analysis of DEP force in the x
 266 direction. To validate this explicit formulation, the numerical Central Difference Method (CDM) [48, 49, 50]
 267 is used and it is reported in the appendix. The proposed sensitivity analysis is generic. Following the same
 268 procedure, one can find a similar formulation for optimizing the DEP force in the y direction in equation (14)
 269 or a weighted sum of the objective functions in x and y directions that can accurately define the direction
 270 of the DEP force. In addition, the extension to the third dimension is very straightforward. Therefore, the
 271 proposed method to derive the sensitivity analysis can be used for topology optimization of the electrodes
 272 in various DEP-based applications.

273 3.2.3. Sensitivity analysis (electric field)

274 Whether the electric field is considered in the objective function or as a constraint in the optimization
 275 formulation, the derivative of electric field with respect to optimization variable should be calculated for
 276 gradient-based optimization. To do so, the equation (17) for the magnitude of the electric field can be
 277 rewritten as

$$\bar{E}_\Omega = \bar{\Upsilon}^T K \Phi + \sum_e \sum_{i=1}^3 \sum_{j=1}^3 W_i W_j \left[2\phi^T B_x^T(\xi_i, \eta_j) B_x(\xi_i, \eta_j) \phi + 2\phi^T B_y^T(\xi_i, \eta_j) B_y(\xi_i, \eta_j) \phi \right] |\bar{J}| \quad (31)$$

278 As you can see in equation (31), we augmented the equilibrium equation (10) to variable \bar{E}_Ω once again
 279 to avoid the calculation of ϕ' . In this case, $\bar{\Upsilon}$ is the global adjoint vector where $(\bar{\cdot})$ is to avoid the confusion
 280 with the previous adjoint vectors. Now, the derivative of \bar{E}_Ω in the elemental format can be calculated as
 281 follows

$$\bar{E}'_\Omega = \bar{\lambda}^T k \phi' + \bar{\lambda}^T k' \phi + \sum_e \sum_{i=1}^3 \sum_{j=1}^3 W_i W_j \left[4B_x^T(\xi_i, \eta_j) B_x(\xi_i, \eta_j) \phi' + 4B_y^T(\xi_i, \eta_j) B_y(\xi_i, \eta_j) \phi' \right] |\bar{J}| \quad (32)$$

282 where $\bar{\lambda}$ is the elemental adjoint vector. Then, the following adjoint equation should be solved to avoid the
 283 calculation of ϕ'

$$\Upsilon^T K = \sum_e \sum_{i=1}^3 \sum_{j=1}^3 W_i W_j \left[4B_x^T(\xi_i, \eta_j) B_x(\xi_i, \eta_j) + 4B_y^T(\xi_i, \eta_j) B_y(\xi_i, \eta_j) \right] |\bar{J}| \quad (33)$$

284 Equation (33) should be solved at the global level. Therefore, we define,

$$\sum_{i=1}^3 \sum_{j=1}^3 W_i W_j \left[4B_x^T(\xi_i, \eta_j) B_x(\xi_i, \eta_j) + 4B_y^T(\xi_i, \eta_j) B_y(\xi_i, \eta_j) \right] |\bar{J}| = \mathbf{B}_{E,e} \quad (34)$$

285 and matrix $\mathbf{B}_{E,e}$ is a square symmetric matrix at the elemental level with the same dimension as the elemental
286 dielectric matrix and should be assembled to form the global level matrix as follows

$$\sum_e \mathbf{B}_{E,e} = \mathbb{B}_E \quad (35)$$

287 Now, the adjoint equation (33) can be solved in the global level

$$\Upsilon^T K = \Phi^T \mathbb{B}_E \quad (36)$$

288 Finally, with finding the adjoint vector, the sensitivity of \bar{E}_Ω with respect to permittivity can be found by

$$\bar{E}'_\Omega = \bar{\lambda}^T k' \phi \quad (37)$$

289 Equations (37) and (36) forms the sensitivity analysis for the total magnitude of the electric field. The
290 verification of this sensitivity analysis with central difference method is reported in the appendix.

291 After defining the sensitivity analysis, the gradient-based numerical solvers can be employed to update
292 the optimization variables. To do so, the optimization problem should be formulated.

293 3.3. Formulation of optimization

294 The optimization problem is formulated by the definition of the objective function, constraints and opti-
295 mization variables. The objective function is the maximization of the DEP force in a desired direction in a
296 desired area. There will be constraints on the surface area or volume with a constant thickness of the elec-
297 trode and a constraint on the sum of the electric field (\bar{E}_Ω) in the desired area. The optimization variables
298 will be the permittivity of each element in the design domain (γ_i). Now, the optimization problem can be
299 formulated as

$$\begin{aligned} \min \quad \mathbb{J} &= W_x \bar{G}_{x-\Omega} + W_y \bar{G}_{y-\Omega} \quad (W_x + W_y = 1) \\ \text{Subject to} \quad V(\gamma) &= \sum_{i=1}^{NE} \gamma_i v_i \leq V \\ \bar{E}_\Omega &< \bar{E}_d \\ 0 < \gamma_i &\leq 1 \end{aligned} \quad (38)$$

300 In optimization problem (38), the DEP force can be maximized in a particular direction by tuning the
301 weighting factors (W_x) and (W_y). $\bar{G}_{y-\Omega}$ is the maximization of the DEP force in the y direction in the
302 target area (Ω) (i.e. $\bar{G}_{y-\Omega} = \int_{\Omega} \frac{\partial}{\partial y} (E_x^2 + E_y^2) d\Omega$). V is the fraction of the total design volume and v_i is the

303 volume of each element. For the SIMP topology optimization, to steer the gray elements to black or white,
 304 a constraint on the volume of the material is defined in general [20, 24]. This volume constraint shows the
 305 ratio between the volume of the material to the overall volume allowed in the design domain. \bar{E}_d is the
 306 maximum allowable sum of electric field magnitudes (\bar{E}_Ω). The constraint on the optimization variables is
 307 already defined in equation (18).

308 With the formulation of the optimization problem, we can build the SIMP topology optimization algo-
 309 rithm to optimize the topology of the electrode.

310 3.4. Algorithm

The SIMP topology optimization algorithm which has been coded in MATLAB can be written as follows,

Algorithm 1: SIMP topology optimization algorithm for DEP-based applications

- 1 Define the geometrical and material properties, weighting factors, penalization factor, volume fraction, filtering and continuation parameters ;
 - 2 Calculate elemental dielectric matrix using equation (8) ;
 - 3 Assemble elemental matrices to build the global dielectric matrix;
 - 4 Define the desired convergence zone ;
 - 5 Define the design and void domains ;
 - 6 Define the boundary conditions (Definition of initial areas of known potentials);
 - 7 Prepare the filtering method [51];
 - 8 Prepare the MMA algorithm [34, 35] (Setting initial values; Move limit = 0.1) ;
 - 9 Initial guess for the permittivity of each element γ_i ;
 - 10 **while** *maximum permittivity change* > 0.01 or *loop number* < *maximum loop* **do**
 - 11 Apply projection and density filter [52, 51];
 - 12 Build a new global dielectric matrix based on the updated permittivities;
 - 13 Build a new global equilibrium equation based on (10);
 - 14 Apply boundary conditions [43, 44];
 - 15 Solve the global equilibrium equation (10) and find the system response in terms of potential field;
 - 16 Calculate the electric field and DEP forces;
 - 17 Calculate the objective function \mathbb{J} ;
 - 18 Perform sensitivity analysis based on equations (24-29) and (33-37);
 - 19 Applying the builtin MATLAB function "imfilter" to the sensitivities [52];
 - 20 **end**
 - 21 Update permittivities using sensitivity analysis and MMA algorithm [34, 35];
 - 22 Apply the continuation scheme on the penalty and sharpness factor;
 - 23 Post processing
-

311 Some steps of the algorithm are explained in previous sections. The other steps will be explained here.
 312 In the first line of the algorithm, some parameters should be defined. The parameters and their values are
 313 reported in Table 1. In this table, it can be seen that the initial penalization factor is considered to be 2.
 314 Indeed, this penalization factor has been proposed by Yoon et al. [20]. However, the penalization in our
 315 paper is not constant and it will be increased with the continuation scheme. Based on this continuation
 316 scheme, the penalization will start to increase incrementally after iteration number 50. The incremental
 317 increase is 0.25 in every 10 iterations and the maximum penalization factor is considered to be 6. The
 318 continuation scheme is chosen to facilitate the elimination of intermediate densities (gray elements).
 319

320 The important step of the algorithm is updating the optimization variables in line 20 of the algorithm.
 321 This is where the Method of Moving Asymptotes (MMA) developed by Svanberg [34] is used as the solution
 322 method. The implementation code is the second version which is provided in 2007 [35]. In the filtering
 323 step (line 19), the goal is to remove the numerical problems like mesh dependencies, checkerboard problem
 324 and intermediate densities (gray elements). For the filtering technique, the density filter [24, 47] along with

325 Heaviside projection suggested by Wang et al. [51] is employed. The complete MATLAB implementation
 326 code for this combination of filtering methods is provided by Ferrari et al. [52]. Three parameters in
 327 the filtering part should be defined in the first line of the algorithm known as filter radius, threshold and
 328 sharpness factor which are reported in Table 1. The continuation scheme is again applied to the sharpness
 329 factor. The incremental increase for the sharpness factor is 1 in every 15 iterations which starts after iteration
 330 number 50. The combination of the continuation scheme and projection is efficient in terms of steering
 331 the elements to fully black and white in the sequence of optimization iterations and removing the gray
 332 elements. To stop the iteration loop of the algorithm, the maximum permittivity change between two
 333 successful iterations should be less than 0.01 or the maximum number of iterations should be more than
 334 350.

335 Finally, the last step of the algorithm is post-processing. In this step, the final optimal layout is trans-
 336 ferred to the CAD software using the thresholding method proposed by [46] and locating the boundaries
 337 of coordinates using the method proposed by [53]. The threshold to steer the remaining gray elements to
 338 black and white is considered to be 0.5.

339 4. Numerical case study

340 After establishing the SIMP topology optimization based on the detailed finite element modeling, in this
 341 section, the efficiency of the developed topology optimization methodology is assessed in several numerical
 342 case studies. In these case studies, the efficiency is studied in terms of defining the direction of the DEP
 343 force in a target area, maximizing its magnitude and constraining the magnitude of the electric field.

344 In Fig. 4-(a), the design domain, its initial boundary condition and the target area (Ω) are illustrated.
 345 The direction of the DEP force and the magnitude of the electric field should be optimized in this area. The
 346 part which is in white will not be changed during optimization. The gray area (design domain) on the other
 347 hand will converge to black or white after the implementation of the SIMP topology optimization algorithm.
 348 The constraint on the volume fraction is considered to be 0.5. There are boundaries of the design domain
 349 that are determined as the initial positions of the electrodes. Indeed, priory known potentials with inverse
 350 signs are applied to these boundaries. These initially determined potentials remain unchanged during the
 351 optimization. There are other possibilities for the definition of the initial positions of electrodes and even
 352 their placement can be a part of the optimization problem. This case is very similar to the optimization
 353 of boundary conditions for mechanical compliance problems [24]. However, this is beyond the scope of
 354 this paper. The developed algorithm in MATLAB is used to find the optimal shape of the electrodes. The
 355 sequence of optimization is not illustrated and only the final results are reported for the sake of brevity. In
 356 Fig. 4, different weighting factors (W_x & W_y) are considered for the objective function (38) to determine the
 357 desired direction of the DEP force and constraining the magnitude of the electric field. For each case study,
 358 two cases of with and without the constraint on \bar{E} are considered. \bar{E}_d , is considered to be $\bar{E}/3$ from the case
 359 when there is no constraint on \bar{E}_d . Optimal layouts for the electrodes and potential fields are plotted for the
 360 total design domain while the electric field and DEP forces are plotted inside the target area (Ω) with a color
 361 spectrum that shows the magnitude. The parameters related to this numerical study are reported in Table 1.

362 In case studies (1) and (2) of Fig. 4, the goal is to maximize the DEP force in the x direction while in
 363 the case study (2), there is a constraint on \bar{E} . The optimized electrode layouts are illustrated in panels (b)
 364 and (c). The decrease of the electric field's magnitude in the target area is obvious from panels (n) and (o).
 365 In these panels, the color spectrum is set for the same range. The numerical values of \bar{E} and \bar{E}_d are also
 366 reported. The algorithm successfully set the DEP force in the x direction as they are illustrated in panels
 367 (t) and (u). However, by considering the color spectrum which shows the magnitude of the DEP force, it is
 368 obvious that the decrease in the electric field has been done with the cost of decreasing the magnitude of
 369 the DEP force.

370 In cases (3) and (4), the goal is to set the DEP force in the target area in the y direction. The optimal
 371 layouts are illustrated in panels (d) and (e). Similar to cases (1) and (2), the algorithm successfully set the
 372 DEP force in the Y direction while constraining \bar{E} decreases the DEP force as well. In cases (5) and (6), the
 373 goal is to set the DEP force in the diagonal direction. As can be seen in panels (x) and (y), the DEP force is
 374 aligned in the diagonal direction.

375 The numerical study in this section demonstrates the efficiency of the developed methodology in terms

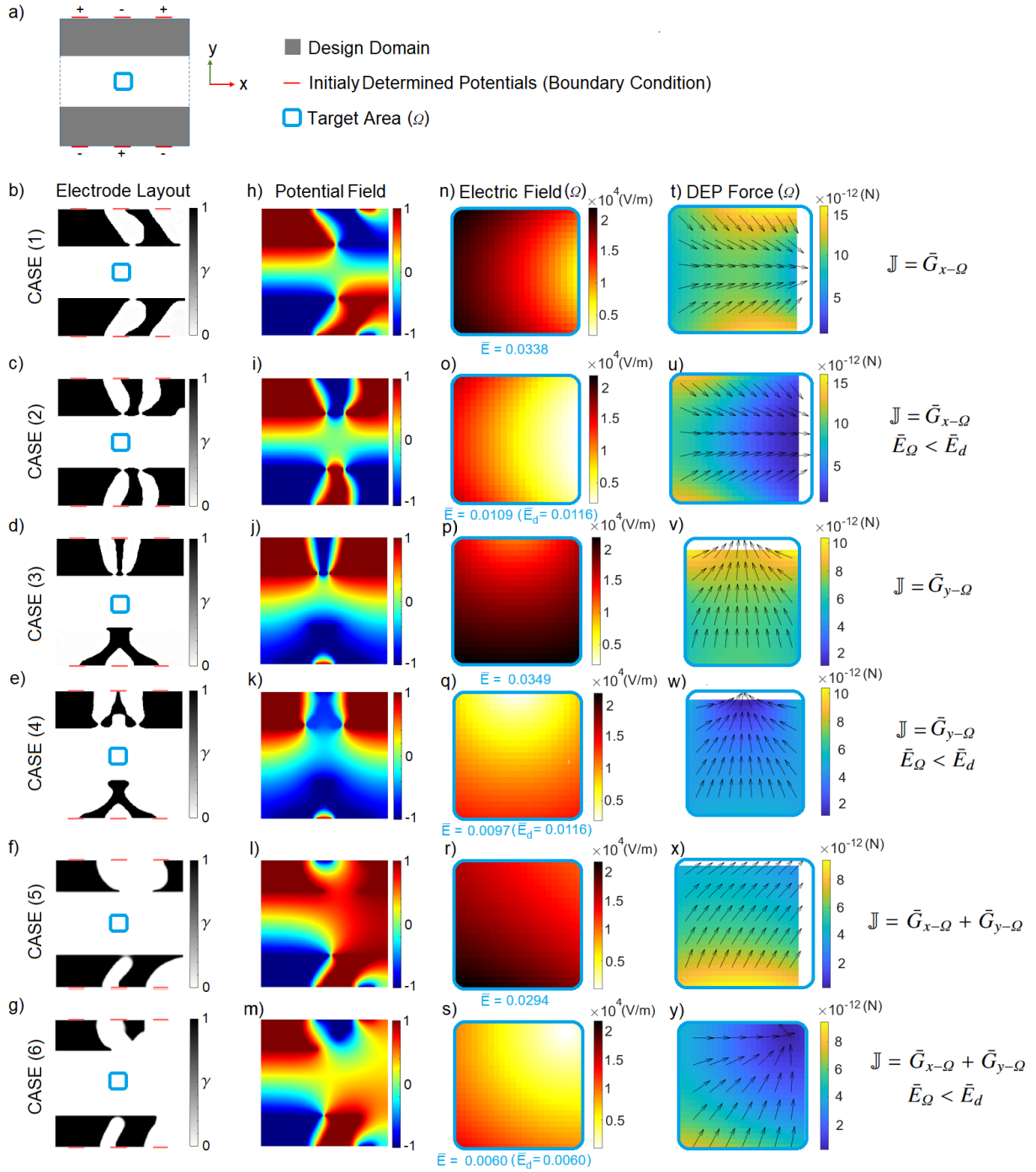


Figure 4: Optimization of electrode layouts to determine the direction of the DEP force and to constrain the electric field. a) Design domain, b-g) Optimal layouts for the electrodes, h-m) Potential field, n-s) Electric field in the target area (Ω), t-y) DEP force in the target area (Ω).

376 of maximizing the magnitude of the DEP force in a particular direction in a target. Moreover, although there
 377 is no control over the local electric field's maximum, constraining the sum of the electric field's magnitude
 378 (\bar{E}) is successful in terms of reducing its magnitude. In the next section, the efficiency of the developed

379 methodology will be investigated experimentally in a practical case study.

380 5. Practical case study: Particle trapping in a microfluidic channel

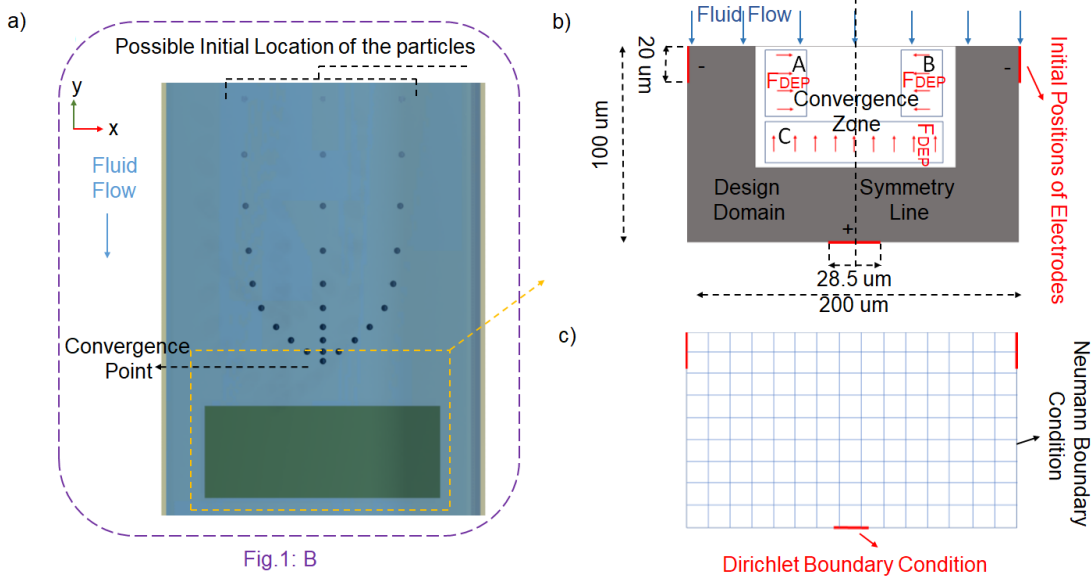


Figure 5: a) Desired trajectory of the particles inside the channel. b) 2 Dimensional representation of the problem c) a coarse discretization of the design domain with imposed boundary conditions.

381 In this section, the goal is to apply the methodology to a particular case study in which the goal is to
 382 trap and stop the particle in a particular region of the channel with the help of DEP force. This case study
 383 has particular interests in cell trapping applications [54, 55] to isolate and analyze the tumor cells in cancer
 384 studies [56]. The graphical representation of this case study is illustrated in Fig. 5-(a). Based on this figure,
 385 if the particles come from certain initial positions in channel, they should converge to a particular region of
 386 interest. This desired region which is located in front of the electrode in the middle of the channel will be
 387 named in the rest of this paper as the convergence zone. Although some basic geometries were suggested
 388 intuitively [14], the idea here is to use topology optimization to find the shape of the electrodes.

389 As it can be seen in Fig. 5-(b), a gray area is considered as the design domain. The initial position of
 390 the electrodes and the sign of applied potentials are defined symmetric to have a symmetrical topology of
 391 electrodes and symmetrical DEP forces after the optimization. The current initial positions for the electrode
 392 are obtained after a trial-error procedure considering different possibilities.

393 By considering the goal of trapping the particles, the directions of the desired DEP forces are illustrated
 394 in Fig. 5-(b). It is desired to maximize the gradient of the electric field in the y direction in the target area C
 395 and in the x direction in the target areas A and B. Keeping into consideration these target areas, the objective
 396 function can be defined as the weighted sum of the electric field gradient for each of the areas,

$$\mathbb{J} = W_x(\bar{G}_{x-\Omega_A} + \bar{G}_{x-\Omega_B}) + W_y\bar{G}_{y-\Omega_C} \quad (39)$$

397 The physical specifications of the channel, electrodes, fluid and particle are mentioned in Table 1. It
 398 should be noted that, in this paper, the FEM and the optimization are done in 2D. This means that the
 399 behavior of the DEP force and the electric field in the third dimension (z axis) is not considered while in
 400 the real application, the behavior of the DEP force in the z direction is also important. Due to the huge fall
 401 of the DEP force in the z direction (height of the channel) which will be discussed in the coming sections,
 402 the objective function (39) is defined to maximize the DEP force and the minimization of the electric field

Parameters (Numerical Study)	Values	Parameters (Particle Trapping)	Values
Permittivity of Electrodes (γ)	$78000\gamma_0$	* CZ Length	$114.28 \mu\text{m}$
Permittivity of Fluid (Water) (γ)	$78\gamma_0$	* CZ Width	$40 \mu\text{m}$
Penalty Factor (p) (initial)	2	Channel Height	$25\mu\text{m}$
Volume Fraction	0.5	Channel width	$310 \mu\text{m}$
Filter Radius	3	Particle Diameter	$10 \mu\text{m}$
Maximum Iteration Loop	350	Particle Permittivity	$2.56\gamma_0$
Threshold	0.8	Design Domain Length	$200 \mu\text{m}$
Sharpness factor (Initial)	2	Design Domain Width	$100 \mu\text{m}$
MMA move	0.1	W_x	0.66
W_E	$1.6e-3$	W_y	0.33

* CZ : Convergence Zone * γ_0 = Permittivity of vacuum

403 is not considered in the practical case study. Moreover, the polystyrene beads are used as particles and not
404 the living cells. Hence, there were no limits for the electric field.

405 6. Optimization results for particle trapping

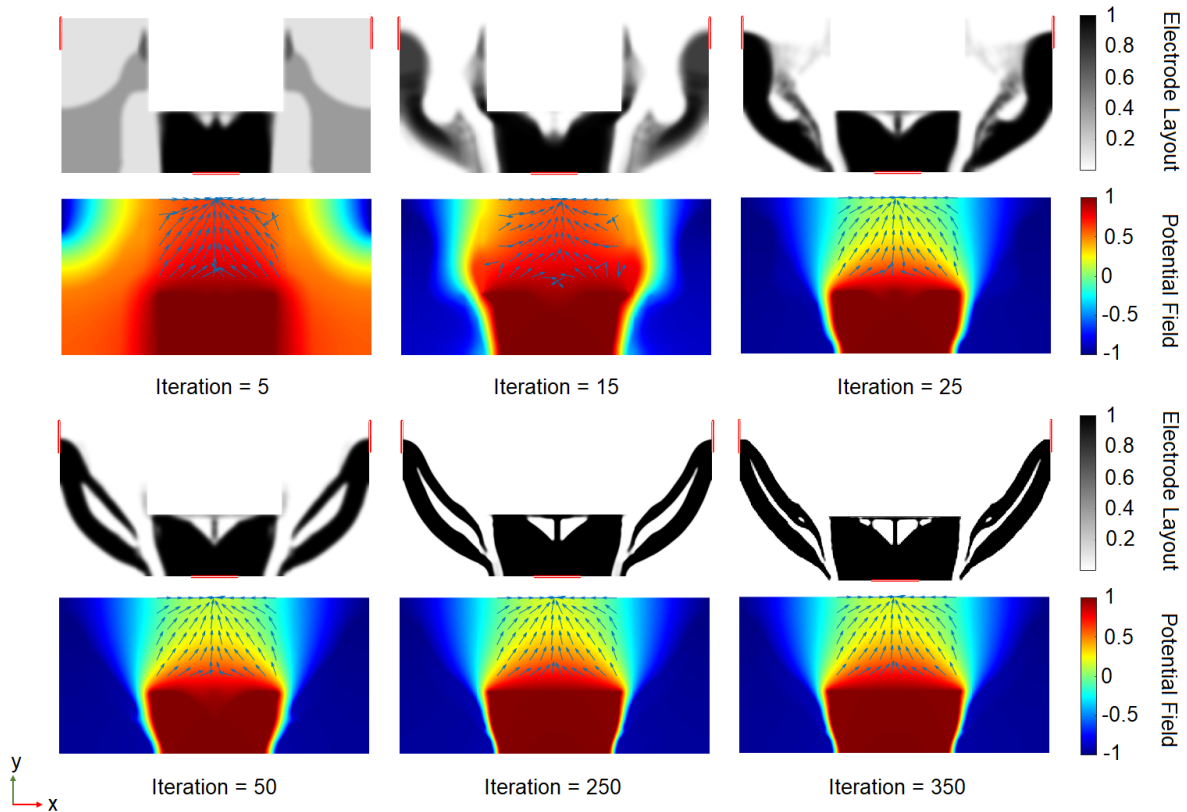


Figure 6: MATLAB topology optimization results for the case of 0.3 volume fraction. Arrows are showing the DEP force direction.

406 To obtain different optimal shapes of the electrodes, two volume fractions of 0.3 and 0.4 are considered
407 here as constraints which gave the best performance among other possible volume fractions. In Fig. 6 and
408 Fig. 7, the MATLAB topology optimization results for these volume fractions are illustrated. The results are
409 shown for certain iterations. The DEP forces in the desired domain of interest converge to the center and

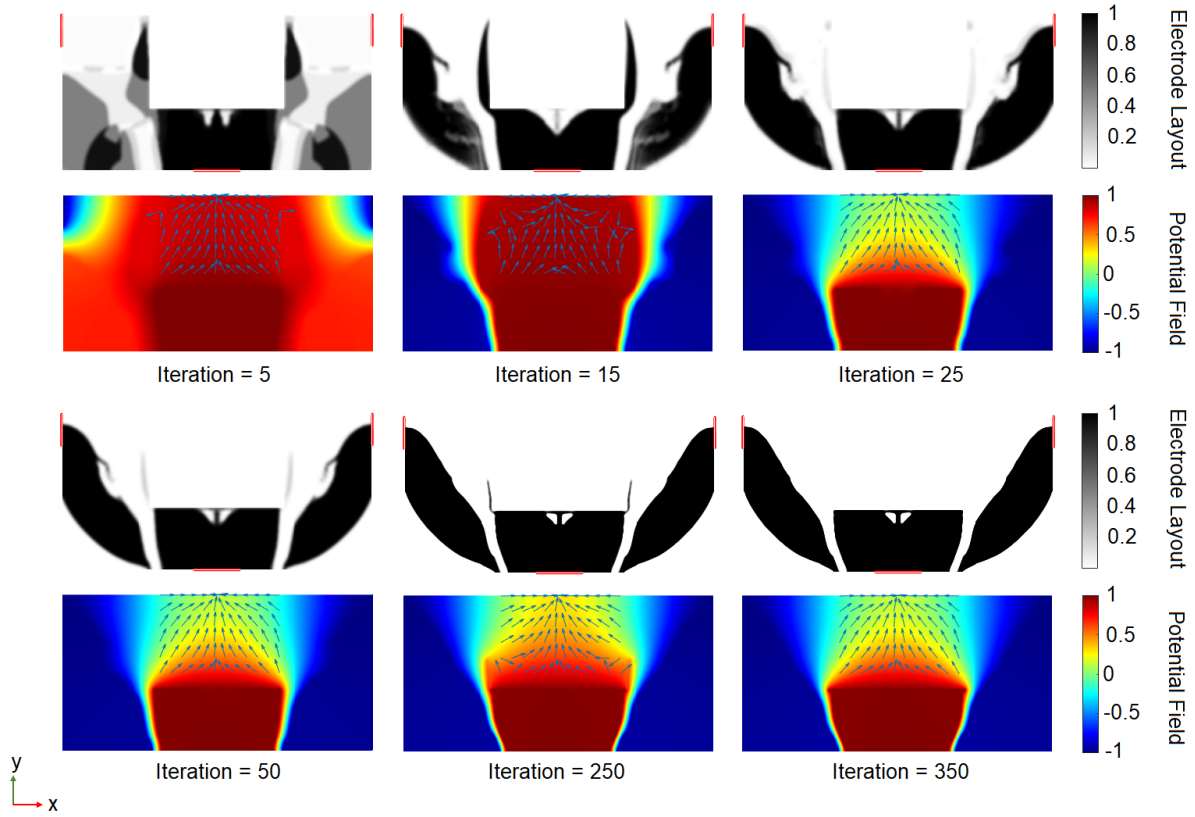


Figure 7: MATLAB topology optimization results for the case of 0.4 volume fraction. Arrows are showing the DEP force direction.

410 toward the inverse direction of the fluid flow which is in accordance with the defined directions of the DEP
 411 forces in Fig. 5-(b). The arrows are normalized to indicate the direction of the DEP force and the amplitude
 412 of the DEP forces will be demonstrated later in the simulation part.

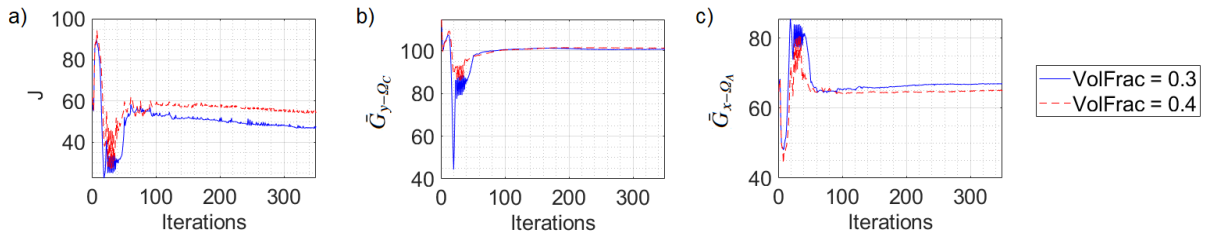


Figure 8: MATLAB optimization data. a) The objective function, b) Square of electric field's gradient in the y direction over the desired area, c) Square of electric field's gradient in the x direction over the desired area.

413 The numerical data of optimization iterations are reported in Fig. 8. For the two volume fractions, $G_{y-\Omega_c}$
 414 is the same. However, for the volume fraction 0.4, a decline in $G_{x-\Omega_c}$ can be seen. For this reason, the
 415 minimization of the objective function (J) shows better results for the volume fraction 0.3. This result shows
 416 that the increase in volume fraction will not necessarily increase the performance of the optimized design
 417 in terms of converging the DEP forces toward the center which is expected in the nonconvex optimization
 418 problem.

419 7. Validation of the obtained designs

420 In this section, the goal is to validate the designs obtained from the MATLAB topology optimization
421 code. As such, this section is divided into two parts of numerical simulation by COMSOL and experimental
422 validation via fabrication of the optimized electrodes. The finite element modeling and optimization in
423 MATLAB have been done with 2D elements. On the other hand, to better understand the actual performance
424 of the optimized design in a real condition, it is necessary to perform the 3D simulation and investigate the
425 efficiency of the optimized design by considering the height of the channel. In order to compare the efficiency
426 of the optimized design with an efficient existing design, a U-shape design inspired from the design which is
427 recently proposed by Punjiya et. al. [36] for cell trapping purposes is also considered during simulation and
428 experiment. It is a 2D electrode that is efficient in trapping particles in the 3D domain of a channel. To make
429 a proper comparison, the modeled U-shape design occupies a similar area to the optimized electrode (0.4)
430 and it is fitted into a similar design domain to the optimized designs. This makes the comparison between
431 the designs fair. Moreover, The chosen design domain gives sufficient freedom to the topology optimization
432 to produce efficient results. To assess the performance of the designs, the potential field and the DEP force
433 in the desired area for trapping the particles are illustrated.

434 7.1. COMSOL 3D simulation

435 The channels, convergence zone and electrodes with geometrical dimensions are illustrated in Fig. 9-
436 (a,f,k). In the rest of the panels of Fig. 9, the directions of the DEP force and electric field are illustrated
437 with the help of the streamlines. For the DEP force, the stream lines are just illustrated in the convergence
438 zone for the purpose of better visualization. The color of the streamlines shows the magnitudes with the
439 help of the color bar.

440 By analyzing the plots in Fig. 9, it can be seen that in the optimized designs the direction of the DEP force
441 is toward the center and opposite to the direction of the flow. This was the predetermined target to trap the
442 particles in the convergence zone. Indeed the stream lines are following the same patterns of the DEP forces
443 in the 2D modeling of Figs. 6 and 7. This proves that the 2D modeling of electrodes is adequately close
444 to their 3D behavior. The only influential factor is the height of the channel which will be discussed later.
445 The same behavior of the DEP force can be seen for the U-shape design but the important point is that we
446 placed the convergence in such a way that it overlaps with the electrode surface. Indeed, the U-shape design
447 produces the maximum amount of DEP force on the face of the electrode while the optimized designs are
448 still capable of producing a satisfactory amount of DEP force in the convergence zone far from the electrode
449 surface. This point can be seen in the panels (e-j-o) of Fig. 9. The amount of electric field for the optimized
450 designs in the convergence zone is less than the U-shape in its convergence zone. By analyzing the DEP
451 force for the U-shape in the z direction, it is obvious that the U-shape pushes the particles to the bottom of
452 the channel while the optimized designs push the particles toward the top of the channel. In this regard,
453 the U-shape is superior to the optimized designs since the DEP force is stronger close to the surface of the
454 electrodes. This is because, in the 2D optimization, the behavior of the DEP force is not considered in the Z
455 direction.

456 To better understand the behavior of DEP force in the direction of the channel's height, the DEP forces
457 are plotted for certain points in Fig. 10. In this figure, two series of points in the direction of the channel's
458 height are considered in two different positions as can be seen in panel (d) of the figure. The first series of
459 points which are marked with blue color is in the center of the channel in front of the electrode. Another
460 series of points which are marked by red color is a bit far from the center and close to the wall of the desired
461 convergence zone. In panels (a) to (c) of Fig. 10, the magnitude of the DEP forces in 3 directions for all
462 the points for the 3 different designs are depicted. For all the directions, the drop in the magnitude of all
463 DEP forces can be seen by going far from the electrode to the top of the channel. Just the DEP force in the
464 z direction has a peak in the 10 μm and then it drops. The most important plot is the DEP forces in the
465 direction of x which are reported in plot (b). In this plot, the magnitudes of the forces at the side points
466 (red color) drop with the channel's height. This means that, as much as we go far from the electrodes,
467 the convergence performance of the electrodes decays. Since the dimension of the particle is 10 μm , we
468 considered the height of the channel to be 25 μm . Less than this height may not be interesting for the DEP

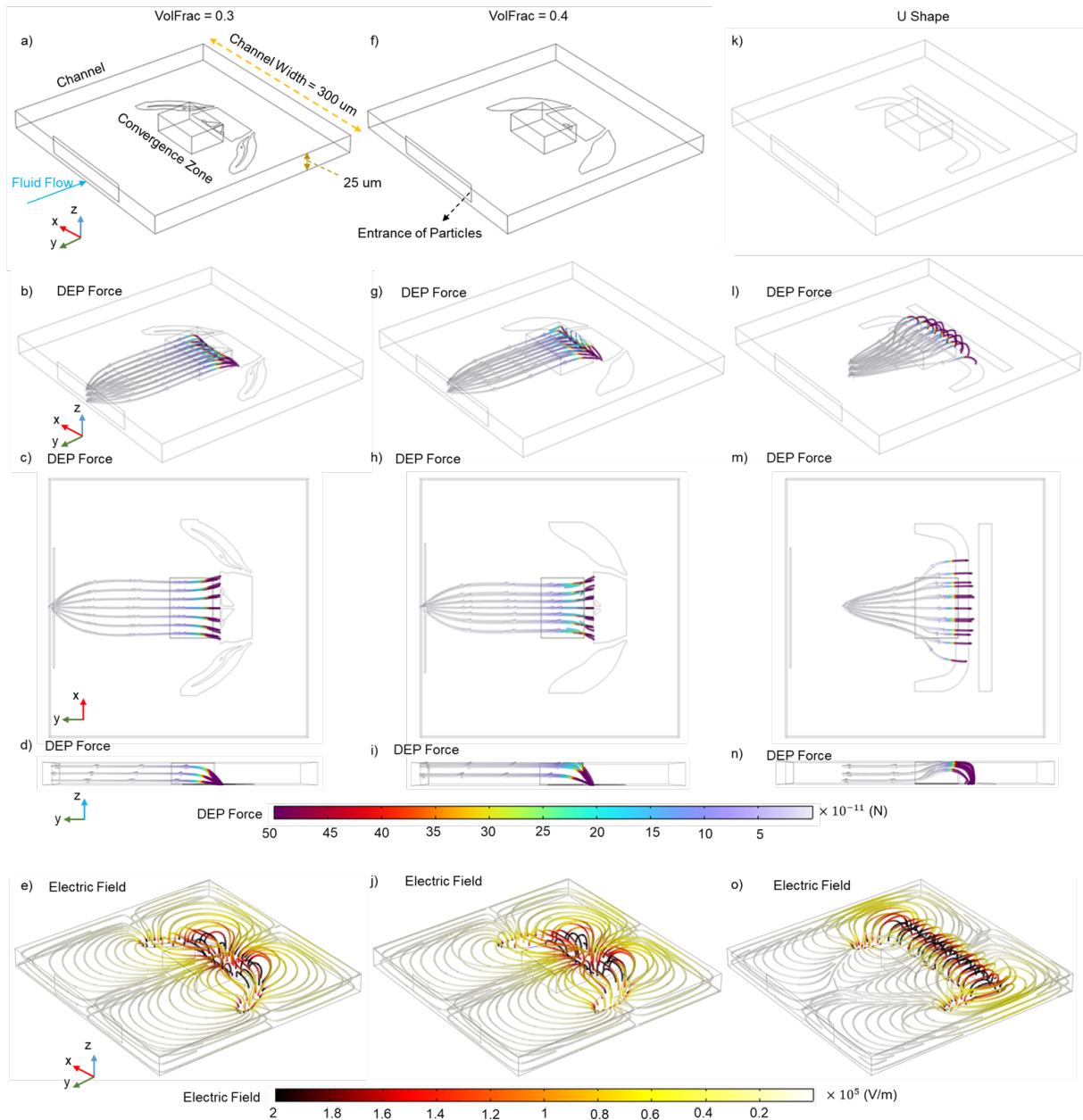


Figure 9: COMSOL 3D simulation results. Stream lines to show the direction and magnitude of the DEP force and the electric field. Colors of stream lines demonstrate the magnitudes referring to color bar.

469 microfluidic chip devices and more than this channel height, based on plots in Fig. 10-(a & b), the drop in
 470 the DEP forces is significant and it may not stop and converge the particles. For the chosen channel height
 471 of 25 μm , the DEP forces at the top of the channel for both the center and side points are reported in Table
 472 2. The analysis of Fig. 10) and the data in Table 2 prove the higher efficiency of the optimized design with
 473 0.3 volume fraction in comparison to other designs. The improvement of design with 0.3 volume fraction
 474 over the U-shape for the side point at the top of the channel is 2.04 and 1.52 for the y and x DEP forces
 475 respectively.

Table 2: Numerical results for the simulation of DEP forces at the top of the channel (height $25 \mu\text{m}$) based on Fig. 10

Center				
Design	$F_{DEP X}(\text{N})$	Impr	$F_{DEP Y}(\text{N})$	Impr
0.3 (Volfrac)	$5.672e^{-12}$	3.18	$1.130e^{-10}$	1.77
0.4 (Volfrac)	$3.039e^{-12}$	1.70	$1.190e^{-10}$	1.89
U-shape	$1.783e^{-12}$	-	$0.627e^{-10}$	-
Side				
Design	$F_{DEP X}(\text{N})$	Impr	$F_{DEP Y}(\text{N})$	Impr
0.3 (Volfrac)	$6.608e^{-12}$	1.527	$1.347e^{-10}$	2.04
0.4 (Volfrac)	$-3.43e^{-12}$	-0.79	$1.190e^{-10}$	1.808
U-shape	$4.325e^{-12}$	-	$0.658e^{-10}$	-

* Impr = Improvement over U-Shape

7.2. Video Simulations

To better investigate the performance of the optimized designs in terms of trapping the particles in the microfluidic channel of Fig. 9-(a), 3D video simulations are provided by using COMSOL multiphysics. In these simulations, the fluid flow inside the channel is modeled by a laminar flow. The fluid is considered to be water with the speed of $300 \mu\text{m}/\text{sec}$. Voltages are applied to the electrodes to produce non-uniform electric field and DEP force. The particles are beads (Polystyrene) with $10 \mu\text{m}$ diameter.

In the video simulations the trapping performances of the optimized designs and the U-shape design can be seen. The entrance of the particles into the channel is considered to be bigger in terms of the width in comparison to the convergence zone which let us see different outcomes based on the initial position of particles. Optimized designs are successfully trapping all the particles coming to the convergence zone. Moreover, they will be pushed to the center of the channel in the direction of x. Other particles that did not enter to the convergence zone, are trapped in other places which are not predetermined. U-shape design also traps all the particles with two major differences in comparison to the optimized designs. The first major difference is that the U-shape design stops the particles very close to the edge of the electrodes where the electric field is maximum. On the other hand, optimized designs stops the particles far from the edge of the electrodes. This makes the optimized designs superior over the U-shape design. However, the advantage of the U-shape design over the optimized design is that it pushes the particles to the bottom of the channel where the DEP force is maximum while the optimized designs push the particles to the top of the channel where the DEP force is minimum.

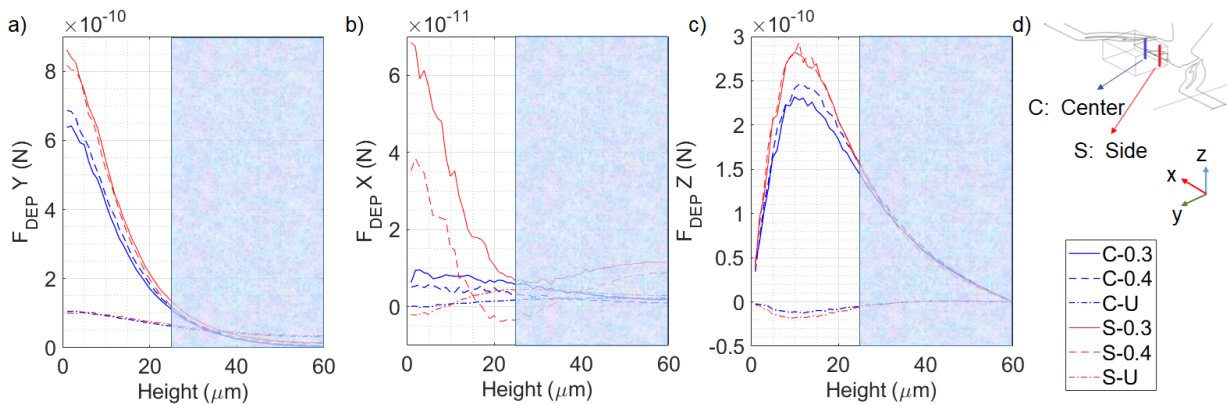


Figure 10: DEP force analysis in the direction of the channel's height. Maximum height of the channel in the experimentation is $25 \mu\text{m}$. However, in this figure, the DEP forces are analyzed for the $60 \mu\text{m}$ channel's height. a) DEP force in the y direction as a function of the channel's height, b) DEP force in the x direction as a function of the channel's height, c) DEP force in the z direction as a function of the channel's height, d) Two possible location for the analysis of the DEP force as a function of channel's height

495 So far, the performance of the optimized design are analyzed and compared to a U-shape design through
 496 3D simulation by COMSOL Multiphysics software. The next step would be the experimental investigation
 497 which requires the fabrication of the proposed designs. This will be the subject of the next section.

498 7.3. Experimental investigation

499 In this section, the performances of the optimized designs are investigated through several experimental
 500 tests. To do so, first, the proposed designs are fabricated on a fluidic chip, using micro-fabrication technology
 501 tools. The substrate of the chip is made of glass and the 200 nm gold electrodes are deposited and patterned
 502 by photo-lithography and the channels are made of SU8 resin as can be seen in Fig. 11-(d-e). Through the
 503 channel, the fluid with particles can flow while a PDMS layer is used to cover the channel. An experimental
 504 bench is set up to flow the fluid and particles inside the channel as it is illustrated in Fig. 11-(a,b,c). The
 505 experimental setup and the microfabrication procedure of the fluidic chip are explained more in detail in
 506 the appendix.

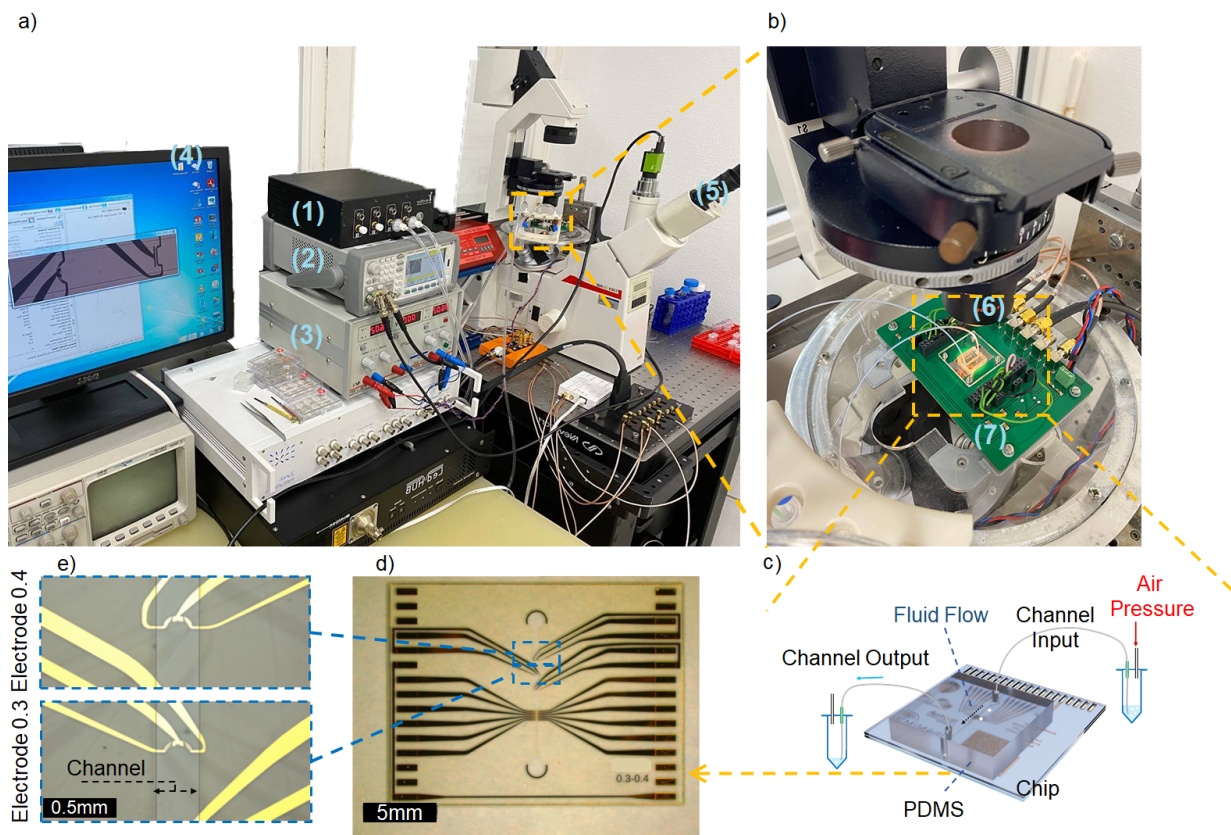


Figure 11: a) Experimental setup, b) Microfluidic chip under the microscope, c) Schematic of the microfluidic chip, d) Fabricated chip in the cleanroom, e) Electrodes magnification under the microscope. Instruments: 1- Air pressure controller, 2- Signal generator, 3- Voltage amplifier, 4- Computer control unit, 5- Microscope, 6- Camera, 7- PCB

507 The trapping performance of the designs has been investigated on the polystyrene microbeads with 10
 508 μm diameter. The results of the experiments are shown in Fig. 12. The recordings of the experiments are
 509 attached as electronic supplementary files. In Fig. 12, several chosen frames for different positions of the
 510 particles are illustrated. As it is obvious in these frames, the particle comes from a point that has a distance
 511 from the center of the channel (x direction). Then, when it comes close to the electrode, its speed decreases.
 512 This is due to the DEP force of the electrode in the y direction. Afterward, the particles shifts slowly to the
 513 center of the channel in front of the electrode and rest in that position. This means that the DEP force in the

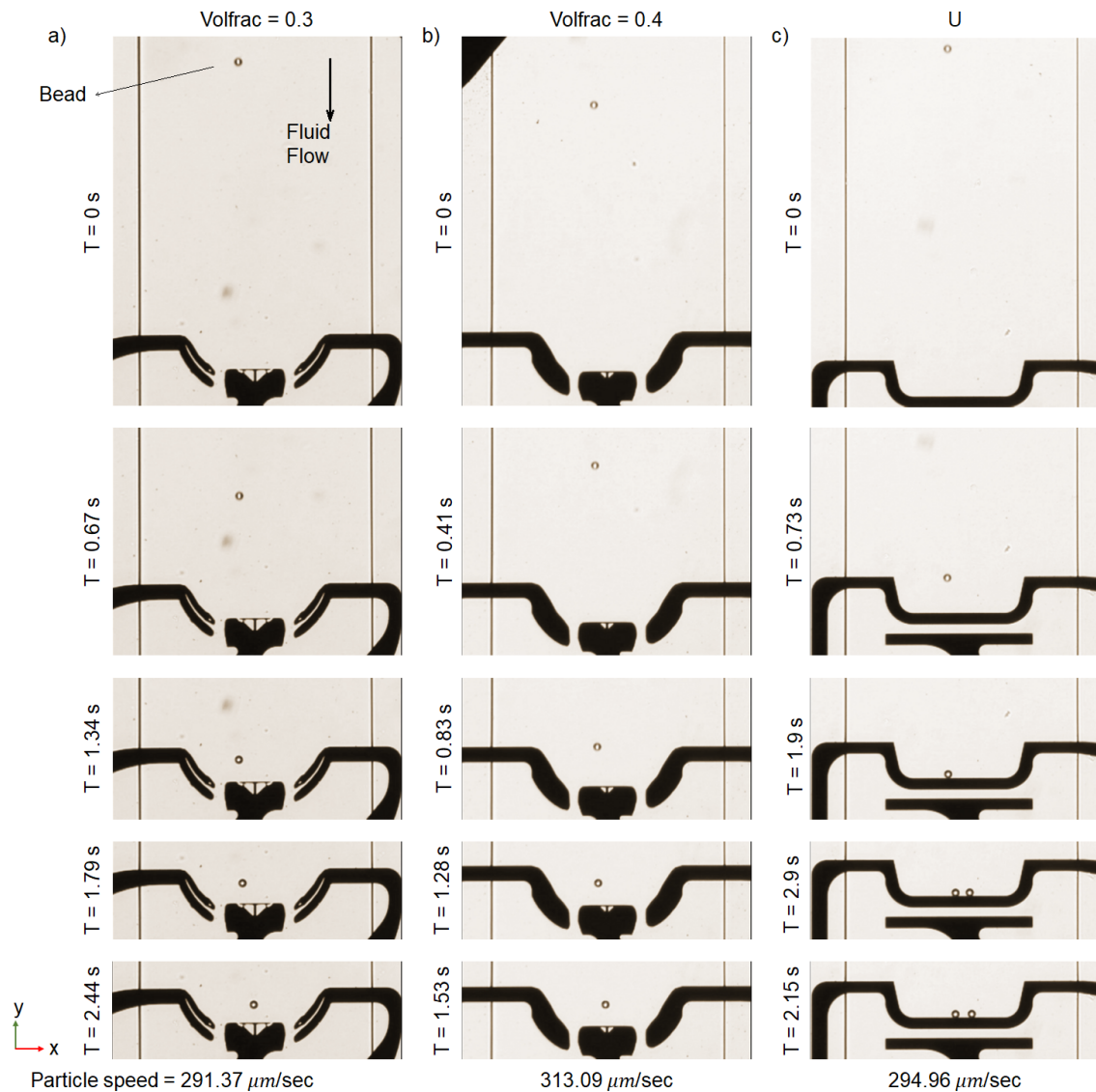


Figure 12: Experimental result for trapping beads. Particles flow inside the channel for three different designs: a) Optimized design with volume fraction 0.3, b) Optimized design with volume fraction 0.4 and c) the U-shape design. T = time (s)

514 x direction pushes the particle to the center and the combination of the DEP forces in the y and x directions
 515 stops the beads at a particular point inside the convergence zone. It can be discovered in Fig. 12 that the
 516 electrodes are corroded due to the electrolysis effect and hence the electrode shapes are not completely the
 517 same as the optimized ones. This is the inevitable effect of having small features in the electrodes.

518 In the experiments, we tried different bead speeds to assess the trapping performance of different designs
 519 as can be seen in the attached video files. However, to compare the performances in Fig. 12, it is tried to
 520 keep the speeds of the beads for different designs close to each other, by controlling the air pressure driving
 521 the fluid flow. The performances of the 0.3 and 0.4 designs are similar to each other in terms of trapping the
 522 bead. The U-shape design stops the beads on the edge of the electrode where the electric field is maximum.
 523 This is in accordance to what was seen in the simulation part. In a sequence of tries with different bead
 524 speeds, it was clear that the U-shape design successfully stops the beads against the fluid flow (y direction)

525 on the borders of the electrode. However, the considered U-shape is weak in terms of pushing the particles
526 to the center of the channel in the x direction. This can be due to the fact that the considered U-shape in
527 this paper is a modified (elongated) of the original proposed U-shape [36]. This will be discussed next.

528 8. Discussion

529 In the numerical and practical case studies, we tried to prove the efficiency of the developed methodology
530 in terms of defining the direction of the DEP force and modifying the magnitude of the electric field. On
531 the other hand, a more detailed study can be done on the different design and optimization parameters
532 that can affect the obtained results. For example, volume fraction constraint, initially defined potentials,
533 resolution of the mesh, penalty factor in the interpolation function, radius of the filtering method, changing
534 the sharpness and threshold of the projection, weighting factors in the objective function, etc all can affect
535 the result of optimization. Indeed, it may be possible to obtain more efficient layout of the electrodes than
536 what we have reported in this paper. Here, we developed a methodology for optimal design of electrode's
537 shape. Separated studies are needed to investigate the effects of all the aforementioned parameters.

538 The initially determined potentials can be considered in the optimization problem as well. This needs the
539 definition of additional optimization variables and new sensitivity analysis. This approach will be considered
540 for future studies.

541 In this paper, a constraint is considered on a sum of the electric field's magnitude in a desired area.
542 Although it was successful in reducing the maximum electric field, The better approach can be the consid-
543 eration of the local maximum of electric field in the optimization problem which requires new sensitivity
544 analysis and is considered for future studies.

545 The considered U-shape in this paper has a different geometry from the original U-shape proposed by
546 [36]. The reason for this modification is to keep the surface area and the borders of the domain similar to
547 the design domain of optimization. The chosen design domain provides enough space for the topology op-
548 timization to produce efficient results. It is possible to obtain better performance from U-shape by changing
549 its geometry. On the other hand, this is also true for the results obtained by topology optimization. The
550 idea of comparison with the U-shape is to challenge the proposed methodology against an existing layout.
551 Otherwise, finding the best results by changing the parameters of optimizations is up to readers as explained
552 before.

553 The limits of the developed methodology mainly lie in the fabrication process. The small features that can
554 appear in the optimized electrode design are complicated to fabricate. Moreover, those small features can
555 result in the electrolysis phenomenon when applying the voltage to the electrode that erodes the electrode.
556 The fabrication constraints can be considered in the topology optimization method in future studies. To
557 avoid the small feature in the obtained design one can increase the filter radius as an optimization parameter.

558 The size of the beads in the experiments is chosen to be $10 \mu m$ which is close to the size of the biological
559 cells including lymphocytes in the medical therapy devices. We demonstrated that for this size of the beads
560 and the channel height of $25 \mu m$, the DEP force is strong enough to stop the beads. For higher channel
561 height, the convergence efficiency of the electrodes will drop due to the low magnitude of the DEP force.
562 This can be ameliorated by considering the electrodes on the top and bottom of the channel. Consequently,
563 the generality of the proposed approach remains intact.

564 9. Conclusion

565 In this paper, a detailed FEM is employed to model the DEP force and electric field induced by elec-
566 trodes. Based on this FEM, a general optimization problem is formulated to determine the direction of the
567 DEP force, maximize its magnitude and minimize the magnitude of the electric field. SIMP topology opti-
568 mization approach is implemented by deriving the explicit formulation of the sensitivity analysis to perform
569 a gradient-based optimization. The performance of the methodology is assessed in several numerical case
570 studies. It has been demonstrated that the developed optimization methodology can optimize the shape
571 of the electrode in order to determine the direction of the DEP force and minimize the magnitude of the
572 electric field. After numerical investigation, the performance of the methodology is demonstrated in a real
573 practical application. It has been demonstrated by 3D COMSOL simulation that optimized 2D electrode is
574 efficient enough for a limited height of the channel. This is later approved by experimental investigation

575 and the efficiency of the optimized electrode is demonstrated in comparison to an electrode design similar
 576 to the layout existing the literature.

577 The future perspective of the research can be the extension of the FEM approach from 2D to 3D. In this
 578 way, the behavior of the DEP force in the direction of the channel's height can be taken into consideration
 579 in the optimization problem. Moreover, designing the 3D electrodes on all surfaces of the channel instead
 580 of considering them just at the bottom of the channel can be done with the help of 3D modeling and
 581 optimization while doing so intuitively is considerably challenging.

582 **Conflicts of interest**

583 There are no conflicts to declare.

584 **Acknowledgements**

585 This work was supported in part by the EIPHI Graduate School under Contract ANR- 17-EURE-0002, in
 586 part by the MiMedi project funded by BPI France under Grant DOS0060162/00 and by the European Union
 587 through the European Regional Development Fund of the Region Bourgogne-Franche-Comté under Grant
 588 FC0013440 and in part by the french RENATECH network and its FEMTO-ST technological facility.

589 **Appendix**

590 *Reminder of Finite element method*

591 In this section, we will remind the important part of the finite element method which is necessary for
 592 modeling and sensitivity analysis in this paper.

593 The goal here is to calculate the electric field and its gradient based on the natural coordinates of the
 594 square parent element. To begin with, the gradient interpolation matrix mentioned in equation (7), can be
 595 expressed as

$$B = \begin{bmatrix} B_\xi \\ B_\eta \end{bmatrix} = \begin{bmatrix} b_{1,1}(\xi, \eta) & b_{1,2}(\xi, \eta) & \dots & b_{1,8}(\xi, \eta) \\ b_{2,1}(\xi, \eta) & b_{2,2}(\xi, \eta) & \dots & b_{2,8}(\xi, \eta) \end{bmatrix} \quad (40)$$

596 In this equation, ξ and η are the natural coordinates as it has been shown in Fig. 3-(d). $b_{i,j}(\xi, \eta)$ in
 597 equation (40) is the derivation of the shape functions with respect to the natural coordinates. The shape
 598 functions of the 8 node rectangular element and their derivatives can be found in [45].

599 The calculation of gradient interpolation matrix is now used to calculate the elemental dielectric matrix.

$$k = \int_{\Omega^e} B^T \varepsilon B d\Omega = \int_{-1}^{+1} \int_{-1}^{+1} B^T \varepsilon B |\bar{J}| d\xi d\eta \quad (41)$$

600 in which $|\bar{J}|$ is the determinant of the Jacobean matrix to map the coordinate system from global coordinate
 601 to the natural coordinate [42]. The integration over each element can be done using the numerical Gauss
 602 quadrature method [42]. Moreover, the calculation of gradient interpolation matrix is used in calculation of
 603 the decomposition of electric field as it is mentioned in equation (11). However, The gradient interpolation
 604 matrix (B) is right now based on the natural coordinate system while we need the gradient interpolation
 605 matrix in the global coordinates. Since we are using the rectangular element to discretize the design do-
 606 main which is a particular form of quadrilateral elements, transferring from natural coordinates to global
 607 coordinates is straightforward [42],

$$\begin{aligned} \frac{\partial}{\partial x} &= \frac{\partial}{\partial \xi} \frac{\partial \xi}{\partial x} = \frac{1}{le} \frac{\partial}{\partial \xi} \\ \frac{\partial}{\partial y} &= \frac{\partial}{\partial \eta} \frac{\partial \eta}{\partial x} = \frac{1}{we} \frac{\partial}{\partial \eta} \end{aligned} \quad (42)$$

608 Therefore, the vector of electric field for each element can be calculated as

$$\begin{bmatrix} E_x \\ E_y \end{bmatrix} = \begin{bmatrix} \frac{1}{le} & 0 \\ 0 & \frac{1}{we} \end{bmatrix} \begin{bmatrix} B_\xi \\ B_\eta \end{bmatrix} \begin{bmatrix} \phi_1 \\ \phi_2 \\ \phi_3 \\ \phi_4 \\ \phi_5 \\ \phi_6 \\ \phi_7 \\ \phi_8 \end{bmatrix} \quad (43)$$

609 and gradient interpolation matrices can be expressed as

$$B_x = \frac{1}{le} B_\xi, \quad B_y = \frac{1}{we} B_\eta \quad (44)$$

610 The crucial part in our finite element modeling and calculation of DEP force is the Gradient of the electric
611 field. Using the natural coordinates, the derivatives if the electric fields can be calculated as,

$$\begin{aligned} \frac{\partial}{\partial y} E_x &= \frac{\partial}{\partial y} B_x \phi = \frac{1}{we} \frac{\partial}{\partial \eta} B_x \phi = B_{x,y} \phi \\ \frac{\partial}{\partial y} E_y &= \frac{\partial}{\partial y} B_y \phi = \frac{1}{we} \frac{\partial}{\partial \eta} B_y \phi = B_{y,y} \phi \\ \frac{\partial}{\partial x} E_x &= \frac{\partial}{\partial x} B_x \phi = \frac{1}{le} \frac{\partial}{\partial \xi} B_x \phi = B_{x,x} \phi \\ \frac{\partial}{\partial x} E_y &= \frac{\partial}{\partial x} B_y \phi = \frac{1}{le} \frac{\partial}{\partial \xi} B_y \phi = B_{y,x} \phi \end{aligned} \quad (45)$$

612 These relations, makes the calculation of the gradient of electrical field in equation (13) straightforward.

613 *Validation of the developed FEM*

614 To validate the developed FEM in this paper, the results obtained by MATLAB are compared to the ones
615 from COMSOL multiphysics. In Fig. 13, the potential field, electric field and the DEP force for the two
616 optimized designs which are calculated by MATLAB are compared with COMSOL FEM results. In panels (d)
617 and (e), the color spectrum demonstrates the magnitude of electric field. In panels (g) and (h) of Fig. 13 the
618 color spectrum shows the magnitude of the DEP force and arrows represent the direction of the DEP force.
619 The numerical values of the two methods are calculated on a particular line which is chosen randomly and
620 are plotted in panels (c), (f) and (i) of Fig. 13.

621 The agreement between the developed FEM in MATLAB and the FEM in COMSOL for potential and
622 electric field is quite satisfying. For the DEP force, MATLAB demonstrates a jump in the magnitude of the
623 DEP force at the borders of the electrode. The reason is that, at the borders of the electrodes there is a
624 sudden change in the potential and with a two times derivation it manifests as a high value. This jump
625 is not seen in the COMSOL software due to change in the mesh size at the borders of the electrode. In
626 fact, COMSOL is using a mesh with variable size triangular elements to discretize the design domain and
627 it captures the edge more precisely while in MATLAB we are using constant size rectangular elements and
628 there are huge changes in the potential values in one element which manifest high values in the second
629 derivation with respect to potential.

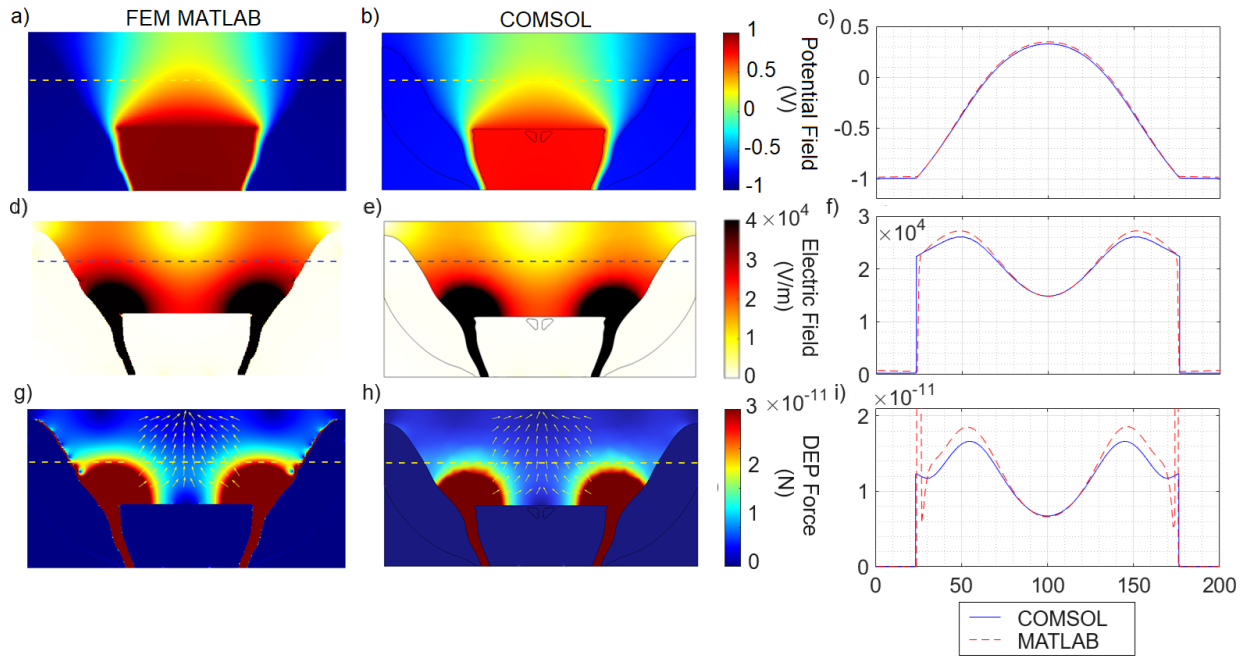


Figure 13: Validation of developed FEM for potential and electric fields and DEP force. Arrows represents the normalized DEP force. a), d) and g), FEM developed in MATLAB. b), e) and h), COMSOL simulation. c), f), i) Numerical values are reported over the dash lines.

630 Validation of sensitivity analysis by CDM

631 In Central Difference Method (CDM), the derivative of objective function with respect to the optimization
 632 variables can be calculated using the following equation [48],

$$\frac{d\mathbb{J}(\gamma)}{d\gamma_e} = \frac{\mathbb{J}(\gamma + \Delta h) - \mathbb{J}(\gamma - \Delta h)}{2\Delta h} \quad (46)$$

633 in which Δh is a vector containing zeros for all elements except the one corresponds to element $\{e\}$. With
 634 CDM it is possible to calculate the sensitivities. However, to calculate the sensitivity of each element, the
 635 global equilibrium finite element equation (10) should be solved two times. This makes the calculation of
 636 sensitivities by CDM extremely time consuming. That is why to verify the proposed sensitivity analysis, a
 637 coarse mesh is considered (10×20 elements). The result of sensitivities with two different methods are
 638 reported in Fig. 14 for $\Delta h = 1e^{-6}$. These sensitivities are related to the case study which is illustrated in Fig.
 639 5. The plots show an excellent agreement between two methods and verify the accuracy of the proposed
 640 sensitivity analysis.

641 Fabrication of Fluidic Chip

642 The microfluidic chips are manufactured by the flowchart adapted from [57] which follows a simple
 643 known manufacturing processes. First, $200nm$ of gold is deposited on $20nm$ of titanium (adhesion layer) by
 644 evaporation (*Plassys, EVAP MEB600*) on a borosilicate (BF33) wafer as a substrate. To create the microfluidic
 645 channel, a negative photosensitive resin (*SU-8 3500*) is spin-coated with chosen spin-coating parameters to
 646 reach the desired thickness of the resin i.e. the desired height of the fluidic channel. A mask is laser-written
 647 (*Heidelberg, Laser Lithography System MLA150*) and used for UV exposure to polymerize the walls of the
 648 fluidic channels (*EVG, Aligner DUV* with a specific SU-8 filter, $E = 300mJ$), quickly followed by a post-expose
 649 bake. Then, the wafer is put in a *PGMEA* developer bath for few minutes with strong agitation to discover

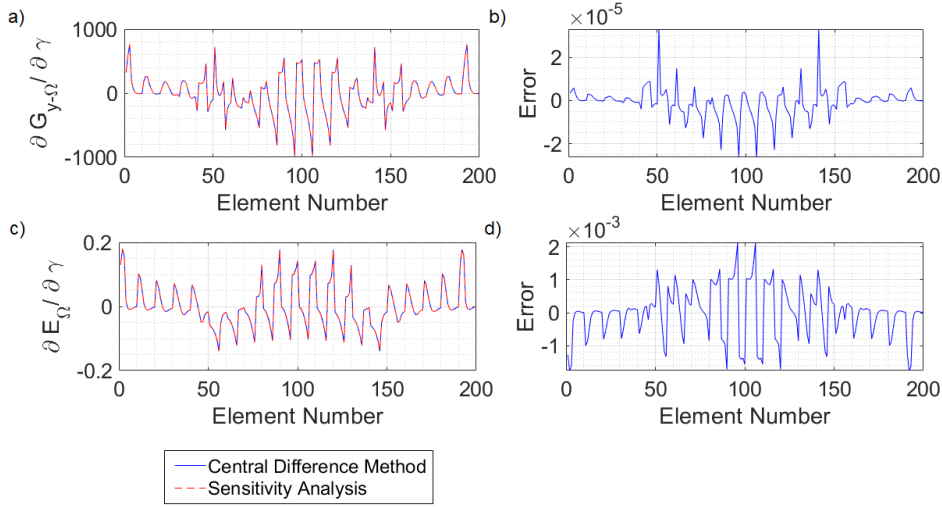


Figure 14: Validation of sensitivity analysis. a,b) Sensitivities calculated by CDM and explicit formulations b,d) Absolute error between two methods

650 the pattern of the fluidic walls, permanently fixed at the end by a hard-bake, preceded by a short plasma
 651 O₂ etching to ensure the cleanliness of the substrate. The wafer is finally cut into the final different chips
 652 (*DISCO, Dicing Saw DAD 3350*) as it is illustrated in Fig. 11-(d & e). All of the electrode designs are
 653 fabricated on one chip to ensure the same particle speed in all the experiments. To seal each microfluidic
 654 chip, a PDMS cover is used, consisting simply a cast PDMS layer of about half a cm thick, cut at the right
 655 dimensions and punched for the fluidic inlet tubing connection. The PDMS is simply pressed on top of the
 656 chip and kept in place by a dedicated screwed plexiglass holder.

657 *Experimental Setup*

658 To apply a specific voltage to each electrode of the microfluidic chip, a homemade PCB is used to plug
 659 and hold the chip (Fig. 11-(b)) and connect its electronic pads to the desired signals. A NI card (PCI-6733)
 660 is used to control the voltage amplitude coming from the computer DC voltage to the NI interface card
 661 (BNC-2110). Another homemade PCB is used to multiply the DC voltage by a shared AC signal (Waveform
 662 Generator *KEYSIGHT 33500B Series*) at 100kHz, whose amplitude is set to 6V. The generated AC signal is
 663 then sent to the chip. The experiments are monitored through a camera (*JAI, GO-5000C*) placed on the
 664 microscope (*LEICA DM IRBE, ×10 magnification*). As the homemade PCB holding the chip is fixed on a XYZ-
 665 table under the microscope it is possible to visualize the fluidic channel and adjust the monitoring location
 666 as we are controlling the signals and the fluid flow.

667 The fluidic system is described as follows. An air pressure controller (*Elveflow, OB1 Pressure Controller*)
 668 is used to set a specific air pressure in a sealed fluidic tank (*Eppendorf Tube 2ml*) containing around 100μl
 669 of the solution with the beads. The fluidic microtubing (*Darwin Microfluidic PTFE teflon capillary microtube*
 670 $diameter_{ext} = 760\mu m, diameter_{int} = 300\mu m$) inside the solution is connecting the sealed tank to the chip through
 671 the punched PDMS cover. The same system is used for the fluidic outlet with another tank. Applying stronger
 672 air pressure to the inlet allows the displacement of the fluid inside the microfluidic chip as a laminar flow.
 673 As air bubbles can escape through the porous PDMS cover, the fluidic resistances of the whole fluidic system
 674 are almost constant and the fluid flow remains quite stable with a constant target pressure. Changing the
 675 air pressure changes directly the fluid speed in a few milliseconds. Images are post-treated to find the speed
 676 of the particles.

677 The medium electric properties for the beads: the relative permittivity is $\epsilon_{rm} = 78$ and the electric con-
 678 ductivity is $\sigma_m = 0.16 S/m$. To reach this conductivity value, the beads were suspended in a PBS (Phosphate
 679 Buffered Saline) medium diluted ten times in deionized (DI) water. 0,1% of *Tween20* is also added to keep

References

- [1] H. Pohl, H. Pohl, Dielectrophoresis: the behavior of neutral matter in nonuniform electric fields. 1978, Barsotti, R., Vahey, M., Wartena, R., Chiang, Y.-M., Voldman, J., Stellacci, F. *Small* 3 (2007) 488–499.
- [2] V. Gauthier, A. Bolopion, M. Gauthier, Analytical formulation of the electric field induced by electrode arrays: Towards automated dielectrophoretic cell sorting, *Micromachines* 8 (8) (2017) 253.
- [3] A. Lefevre, V. Gauthier, M. Gauthier, A. Bolopion, Closed-loop control of particles based on dielectrophoretic actuation, *IEEE/ASME Transactions on Mechatronics* (2022).
- [4] T. Kodama, T. Osaki, R. Kawano, K. Kamiya, N. Miki, S. Takeuchi, Round-tip dielectrophoresis-based tweezers for single micro-object manipulation, *Biosensors and Bioelectronics* 47 (2013) 206–212.
- [5] J. Myung, S. Hong, Microfluidic devices to enrich and isolate circulating tumor cells, *Lab on a Chip* 15 (24) (2015) 4500–4511.
- [6] O. O. Saeed, R. Li, Y. Deng, et al., Microfluidic approaches for cancer cell separation, *Journal of Biomedical Science and Engineering* 7 (12) (2014) 1005.
- [7] A. Alazzam, B. Mathew, F. Alhammadi, Novel microfluidic device for the continuous separation of cancer cells using dielectrophoresis, *Journal of separation science* 40 (5) (2017) 1193–1200.
- [8] H. Li, R. Bashir, Dielectrophoretic separation and manipulation of live and heat-treated cells of listeria on microfabricated devices with interdigitated electrodes, *Sensors and actuators B: chemical* 86 (2-3) (2002) 215–221.
- [9] N. Demierre, T. Braschler, R. Muller, P. Renaud, Focusing and continuous separation of cells in a microfluidic device using lateral dielectrophoresis, *Sensors and Actuators B: Chemical* 132 (2) (2008) 388–396.
- [10] L. D'Amico, N. Ajami, J. Adachi, P. Gascoyne, J. Petrosino, Isolation and concentration of bacteria from blood using microfluidic membraneless dialysis and dielectrophoresis, *Lab on a Chip* 17 (7) (2017) 1340–1348.
- [11] P. R. Gascoyne, J. V. Vykoukal, Dielectrophoresis-based sample handling in general-purpose programmable diagnostic instruments, *Proceedings of the IEEE* 92 (1) (2004) 22–42.
- [12] X. Hu, P. H. Bessette, J. Qian, C. D. Meinhart, P. S. Daugherty, H. T. Soh, Marker-specific sorting of rare cells using dielectrophoresis, *Proceedings of the national academy of sciences* 102 (44) (2005) 15757–15761.
- [13] K. Khoshmanesh, C. Zhang, F. J. Tovar-Lopez, S. Nahavandi, S. Baratchi, K. Kalantar-zadeh, A. Mitchell, Dielectrophoretic manipulation and separation of microparticles using curved microelectrodes, *Electrophoresis* 30 (21) (2009) 3707–3717.
- [14] H. Zhang, H. Chang, P. Neuzil, Dep-on-a-chip: Dielectrophoresis applied to microfluidic platforms, *Micromachines* 10 (6) (2019) 423.
- [15] T. Z. Jubery, P. Dutta, A new design for efficient dielectrophoretic separation of cells in a microdevice, *Electrophoresis* 34 (5) (2013) 643–650.
- [16] H. Sadeghian, Y. Hojjat, M. Soleimani, Interdigitated electrode design and optimization for dielectrophoresis cell separation actuators, *Journal of Electrostatics* 86 (2017) 41–49.
- [17] S. Kinio, J. K. Mills, Design of electrode topologies for dielectrophoresis through the use of genetic optimization with comsol multiphysics, in: 2015 IEEE International Conference on Mechatronics and Automation (ICMA), IEEE, 2015, pp. 1019–1024.
- [18] S. Kinio, J. K. Mills, Design of optimal electrode geometries for dielectrophoresis using fitness based on simplified particle trajectories, *Biomedical microdevices* 18 (4) (2016) 1–15.
- [19] C.-H. Han, H. W. Ha, J. Jang, Two-dimensional computational method for generating planar electrode patterns with enhanced volumetric electric fields and its application to continuous dielectrophoretic bacterial capture, *Lab on a Chip* 19 (10) (2019) 1772–1782.
- [20] G. H. Yoon, J. Park, Topological design of electrode shapes for dielectrophoresis based devices, *Journal of Electrostatics* 68 (6) (2010) 475–486.
- [21] T. B. Napotnik, T. Polajžer, D. Miklavčič, Cell death due to electroporation—a review, *Bioelectrochemistry* 141 (2021) 107871.
- [22] M. P. Bendsoe, N. Kikuchi, Generating optimal topologies in structural design using a homogenization method, *Computer Methods in Applied Mechanics and Engineering* (1988).
- [23] H. Zhang, Y. Wang, Z. Kang, Topology optimization for concurrent design of layer-wise graded lattice materials and structures, *International Journal of Engineering Science* 138 (2019) 26–49.
- [24] M. P. Bendsoe, O. Sigmund, *Topology optimization: theory, methods, and applications*, Springer Science & Business Media, 2003.
- [25] T. Dbouk, A review about the engineering design of optimal heat transfer systems using topology optimization, *Applied Thermal Engineering* 112 (2017) 841–854.
- [26] Y. Chen, S. Zhou, Q. Li, Multiobjective topology optimization for finite periodic structures, *Computers & Structures* 88 (11-12) (2010) 806–811.
- [27] J. Alexandersen, C. S. Andreasen, A review of topology optimisation for fluid-based problems, *Fluids* 5 (1) (2020) 29.
- [28] K. A. James, G. J. Kennedy, J. R. Martins, Concurrent aerostructural topology optimization of a wing box, *Computers & Structures* 134 (2014) 1–17.
- [29] R. E. Christiansen, O. Sigmund, Compact 200 line matlab code for inverse design in photonics by topology optimization: tutorial, *JOSA B* 38 (2) (2021) 510–520.
- [30] A. Homayouni-Amlashi, A. M. Ousaid, M. Rakotondrabe, Multi directional piezoelectric plate energy harvesters designed by topology optimization algorithm, *IEEE Robotics and Automation Letters* (2019).
- [31] A. Homayouni-Amlashi, A. Mohand-Ousaid, M. Rakotondrabe, Topology optimization of 2dof piezoelectric plate energy harvester under external in-plane force, *Journal of Micro-Bio Robotics* (2020) 1–13.
- [32] A. Homayouni-Amlashi, T. Schlinquer, A. Mohand-Ousaid, M. Rakotondrabe, 2d topology optimization matlab codes for piezoelectric actuators and energy harvesters, *Structural and Multidisciplinary Optimization* 63 (2) (2021) 983–1014.

- [33] Y. Li, L. Liu, S. Yang, Z. Ren, Y. Ma, A multi-objective topology optimization methodology and its application to electromagnetic actuator designs, *IEEE Transactions on Magnetics* 56 (2) (2020) 1–4.
- [34] K. Svanberg, The method of moving asymptotes—a new method for structural optimization, *International journal for numerical methods in engineering* 24 (2) (1987) 359–373.
- [35] K. Svanberg, *Mma and gmma-two methods for nonlinear optimization*, vol 1 (2007) 1–15.
- [36] M. Punjiya, H. R. Nejad, J. Mathews, M. Levin, S. Sonkusale, A flow through device for simultaneous dielectrophoretic cell trapping and ac electroporation, *Scientific reports* 9 (1) (2019) 1–11.
- [37] T. B. Jones, *Fundamentals*, Cambridge University Press, 1995, p. 5–33.
- [38] X. Wang, X.-B. Wang, P. R. Gascoyne, General expressions for dielectrophoretic force and electrorotational torque derived using the maxwell stress tensor method, *Journal of electrostatics* 39 (4) (1997) 277–295.
- [39] R. D. Cook, et al., *Concepts and applications of finite element analysis*, John wiley & sons, 2007.
- [40] J.-H. Kim, S.-H. Kang, S. Cho, Shape design optimization of interdigitated electrodes for maximal electro-adhesion forces, *Structural and Multidisciplinary Optimization* 61 (2020) 1843–1855.
- [41] B. Zheng, C.-J. Chang, H. C. Gea, Topology optimization of energy harvesting devices using piezoelectric materials, *Structural and Multidisciplinary Optimization* 38 (1) (2009) 17–23.
- [42] D. V. Hutton, J. Wu, *Fundamentals of finite element analysis*, Vol. 1, McGraw-hill New York, 2004.
- [43] A. C. Polycarpou, *Introduction to the finite element method in electromagnetics*, Synthesis Lectures on Computational Electromagnetics 1 (1) (2005) 1–126.
- [44] R. Bargallo, *Finite elements for electrical engineering*, Universitat Politecnica De Catalunya (2006).
- [45] D. L. Logan, *A first course in the finite element method*, Cengage Learning, 2016.
- [46] K. Maute, O. Sigmund, Topology optimization approaches: A comparative review, *Structural and Multidisciplinary Optimization* 6 (2013) 1031–1055.
- [47] E. Andreassen, A. Clausen, M. Schevenels, B. S. Lazarov, O. Sigmund, Efficient topology optimization in matlab using 88 lines of code, *Structural and Multidisciplinary Optimization* 43 (1) (2011) 1–16.
- [48] R. Alberdi, G. Zhang, L. Li, K. Khandelwal, A unified framework for nonlinear path-dependent sensitivity analysis in topology optimization, *International Journal for Numerical Methods in Engineering* 115 (1) (2018) 1–56.
- [49] J. Jung, J. Hyun, S. Goo, S. Wang, An efficient design sensitivity analysis using element energies for topology optimization of a frequency response problem, *Computer Methods in Applied Mechanics and Engineering* 296 (2015) 196–210.
- [50] S. Cho, J.-Y. Choi, Efficient topology optimization of thermo-elasticity problems using coupled field adjoint sensitivity analysis method, *Finite Elements in Analysis and Design* 41 (15) (2005) 1481–1495.
- [51] F. Wang, B. S. Lazarov, O. Sigmund, On projection methods, convergence and robust formulations in topology optimization, *Structural and multidisciplinary optimization* 43 (6) (2011) 767–784.
- [52] F. Ferrari, O. Sigmund, A new generation 99 line matlab code for compliance topology optimization and its extension to 3d, *Structural and Multidisciplinary Optimization* 62 (4) (2020) 2211–2228.
- [53] T. Schlinquer, A. Mohand-Ousaid, M. Rakotondrabe, Displacement amplifier mechanism for piezoelectric actuators design using simp topology optimization approach, in: *IEEE ICRA*, 2018, pp. 1–7.
- [54] S. H. Kim, M. Antfolk, M. Kobayashi, S. Kaneda, T. Laurell, T. Fujii, Highly efficient single cell arraying by integrating acoustophoretic cell pre-concentration and dielectrophoretic cell trapping, *Lab on a Chip* 15 (22) (2015) 4356–4363.
- [55] J. Yao, G. Zhu, T. Zhao, M. Takei, Microfluidic device embedding electrodes for dielectrophoretic manipulation of cells—a review, *Electrophoresis* 40 (8) (2019) 1166–1177.
- [56] E. Sollier, D. E. Go, J. Che, D. R. Gossett, S. O’Byrne, W. M. Weaver, N. Kummer, M. Rettig, J. Goldman, N. Nickols, et al., Size-selective collection of circulating tumor cells using vortex technology, *Lab on a Chip* 14 (1) (2014) 63–77.
- [57] B. Brazey, J. Cottet, A. Bolopion, H. Van Lintel, P. Renaud, M. Gauthier, Impedance-based real-time position sensor for lab-on-a-chip devices, *Lab on a Chip* 18 (5) (2018) 818–831.